First-principles Thermodynamics of Stacking Faults and Deformation- induced Polymorphs of Metals

A Thesis

Submitted For the Degree of

Master of Science (Engineering)

in the Faculty of Science

by

Meha Bhogra

To my parents and my brother

DECLARATION

I hereby declare that the matter embodied in the thesis entitled "**First-principles Thermodynamics of Stacking Faults and Deformation-induced Polymorphs of Metals**" is the result of investigations carried out by me at the Theoretical Sciences Unit, Jawaharlal Nehru Centre for Advanced Scientific Research, Bangalore, India under the supervision of Prof. Umesh V. Waghmare and that it has not been submitted elsewhere for the award of any degree or diploma.

In keeping with the general practice in reporting scientific observations, due acknowledgement has been made whenever the work described is based on the findings of other investigators.

<div align="right">

———————————

Meha Bhogra

</div>

CERTIFICATE

I hereby certify that the matter embodied in this thesis entitled "**First-principles Thermodynamics of Stacking Faults and Deformation-induced Polymorphs of Metals**" has been carried out by Ms. Meha Bhogra at the Theoretical Sciences Unit, Jawaharlal Nehru Centre for Advanced Scientific Research, Bangalore, India under my supervision and that it has not been submitted elsewhere for the award of any degree or diploma.

<div style="text-align: right;">

Prof. Umesh V. Waghmare

(Research Supervisor)

</div>

Acknowledgements

Ji, Krishnamohan, Summayya, Jayashree, Jagaran, Suchitra, Arpita, for a sound academic-cum-fun environment in the Lab.

It's an appropriate moment to acknowledge *'my secondary labmates' and all-time best buddies*: Priyanka, Sarada, Sona John, Ananthu for the most cherished moments on campus. From *punctuality in coffee-timings*, to discussion on nature's every unique creature; for every outing I had as a 'Chotu' attachment, to their every thoughtful advice and suggestion, their company is inevitably enjoyable. Along with, my sense of belongingness to JNC is strengthened in the company of a wonderful set of friends *on-campus*, Anjali, Kiruthika, Sankalp, Kanwar, Soumya, Chakri, Krishnamohan, Sharmila, Deepak, Vybhav, Milind, Jose, Sunil, Shashank, Nisha, Croor, my *akka* Manpreet, my yoga teacher Rajeshwari, and baby Raksha.

Times at JNC showcased many changing weathers, sometimes hard and sometimes soothing. But one thing that remained same is the sweetness of coffee at Chandreyya. I thank Sharnappa and Shivuu bhaiya for providing that 'sweet cup of coffee' everyday.

I also appreciate the motivating company and a feel of awesomeness with my *off-campus* friends Trapti, Mariam, Harsh, Rahul, Aalo and Madhuri.

I thank my parents and my brother for their eternal support, encouragement and freedom for pursuing a career of my interest.

Contents

List of Figures

List of Tables

Chapter 1

Introduction

Defects in crystals are not just a subject of scientific curiosity rather an important ingredient of solid-state science. This realization is because of the interesting structure-sensitive properties of crystalline solids emanating from the presence of a small concentration of imperfections in an otherwise perfect lattice. Practically, all the mechanical properties of materials are strongly influenced by crystal defects. The complex nature of their study stems from their tendency to lower the symmetry of the lattice, and their occurrence in varying length scales in the real crystals. Disorderliness of a periodic lattice in the vicinity of a few atoms or lattice sites is termed as a *point defect*, and a topological imperfection extending through the crystal forms a *line* or a *planar defect*.

The most important one-dimensional or linear defect is a dislocation. The concept of dislocation as an elastic singularity, first introduced by Volterra (1907), forms a starting point of theory of dislocations. Its acceptance as a

physical entity is marked by the description of edge dislocation by Taylor, Orowan and Polanyi in 1934, and screw dislocations by Burgers in 1939. The presence of stacking faults as an unbounded planar defect in layered structures was conceptualized by Landau and Lifschitz in 1937. In 1949, Heidenreich and Shockley and Frank introduced the concept of bounded stacking fault, where the edge of a fault or the junction of two different faults is called the partial dislocation. Frank, in 1951, introduced the concept of Burgers vector to define a dislocation line and its core structure in a real crystal [1]. The dislocation core, which extends up to a few lattice spacing, is a region of singularity where the continuum elasticity theory cannot be applied. The core properties control the mobility of dislocations, thus influencing the mechanism of plastic deformation in materials [2]. The need to understand the phenomenon of crystal plasticity has necessitated the accurate description of dislocation core structure on the atomic scale.

The underlying theory for the study of physics of materials at the atomic scales is quite well established. First-principles techniques based on quantum density functional theory (DFT) allow material-specific understanding of local structural and electronic properties at the ground state. The real difficulty arises in connecting the details of electronic-structure calculations at the atomic scale to the macroscopic behavior of materials, as observed in experiments. Further, to extend the knowledge of the ground-state properties to finite temperature analysis of crystal defects, by calculating vibrational contributions to free energies, forms an important part of this thesis.

In this thesis, the analysis of mechanical behavior in three technologically important classes of materials is categorized as: (a) study of deformation-induced polymorphism in HCP metals, and (b) investigation of the deformation mechanisms in Ni_3Al relevant to Ni-based superalloys, and (c) faults in three FCC metals viz. Al, Cu and Ni, at the ground state and finite temperatures.

In **Chapter 2**, an overview of first-principles quantum-mechanical methods based on density functional theory (DFT) and density functional perturbation theory (DFPT) is presented. This includes Born Oppenheimer approximation, Hohenberg and Kohn theorems, and Kohn and Sham equations. The algorithm to solve the Kohn-Sham equation for self-consistency and determination of ground state properties is briefly discussed. In the later part of the chapter, I will present two approaches for the calculation of phonons in crystals viz. frozen phonon method and linear response method, and discuss their applicability and limitations.

In **Chapter 3**, I will present a study of deformation-mechanism in an industrially significant hexagonal-closed packed metal, Titanium, known for its exceptionally superior specific strength and excellent corrosion resistance [3]. Two major mechanisms are responsible for deformation in HCP metals: deformation twinning and ordinary dislocation plasticity [4]. For the samples with size in micrometer i.e. d $>1\mu$m, the twinning controls the mechanical behavior of these metals, but for sub-micrometer samples i.e. d $<1\mu$m, studies have demonstrated the dislocation-mediated deformation [5] with strong

crystal-size effects. Thus, in the domain of present work, I focus on the study of high-density generalized stacking faults and their strain-mediated interactions in titanium, leading to very stable deformation-induced polymorphs of titanium. Corroborating the existence of polymorphs in Ti, this work proceeds with unraveling the concept of polymorphism in other HCP metals. Further, a detailed atomic-structure analysis of titanium polymorphs affirms their distinction from the FCC stacking faults in HCP structure.

In **Chapter 4**, I will present a holistic study of deformation mechanism of L1$_2$ structure of Ni$_3$Al (γ'-phase in Ni-based superalloys) with temperature from $0K$ to 80% of its melting temperature ($\sim 1330K$). The L1$_2$ structure of Ni$_3$Al is a major constituent conferring high-temperature strength to the superalloy. Additionally, the γ'-phase shows an increase in the yield strength with temperature up to 800°C (also known as yield stress anomaly, YSA) [6]. The experimental results attribute this phenomenon to the process of cross-slip from {111} octahedral plane to {001} cube plane (Kear and Wilsdorf 1962, Mills, Bauc and Karnthaler 1989). The driving force for the anomaly in flow stress behavior is still debated. First-principles calculations of slip on different crystallographic planes of Ni$_3$Al have been carried out [7–9], but the effects of temperature on the flow stress have not been determined. The first-principles analysis of anisotropy of slip process in Ni$_3$Al, along with the estimation of temperature-dependent fault energies, described in this thesis, is by far the prime study which predicts the possible cause of yield strength anomaly in Ni$_3$Al at elevated temperatures.

In **Chapter 5**, I will present an *ab initio* study of dislocation-mediated planar faults in FCC metals at ground state and elevated temperatures. The feasibility of slip along a particular slip system is determined in terms of the fault energies, local stability, and the atomic structural changes associated with the faulted configurations introduced in the wake of the slip process. Considering the technological relevance, three FCC metals viz. Al, Cu and Ni are considered as model elements for this study. The relevance of this analysis to the observed mechanical behavior in these metals is uncovered, particularly through our estimates of vibrational contributions to fault energies as a function of temperature, from $0K$ to 80% of their respective melting temperatures. Finally, in **Chapter 6**, I will conclude with a general discussion.

Chapter 2

Theoretical Formalism

Materials are composed of nuclei bound together by electrons. Since the typical energy scales for electrons far exceed those associated with the degrees of freedom of the massive nuclei, the lowest energy ground state of the electrons determines the structure of the nuclei, thus precisely reckoning the ground state material-properties viz equilibrium crystal structure, charge density, phase transition between structures, and many others. This keystone concept has guided the the development of accurate, robust methods to treat electronic ground state, hence understanding the structure of materials at the atomic scale.

By far, the most widespread approach for 'first-principles' quantitative calculations of material-structure and properties is density functional theory (DFT). This chapter discusses the formulation of density functional theory, and the underlying independent-particle approximations to address real many-body problems of electrons in materials.

Further, the response of a material to external stimulus, namely, the displacements of nuclei, can be studied from their vibrational spectrum, measured experimentally by inelastic neutron scattering, infra-red absorption, etc. Theoretically, this response can be determined through changes in electronic energies (E_{total}), forces on the nuclei (F_I), and force constants (C_{IJ}) with changes in atomic positions, leading to the calculation of full phonon dispersion curves. The later part of this chapter reviews two approaches of phonon calculations, namely, frozen phonons and linear response [10].

2.1 Introduction

The fundamental hamiltonian for a system of electrons and nuclei is given by:

$$\hat{H} = -\frac{\hbar^2}{2m_e}\sum_i \nabla_i^2 - \sum_{i,I}\frac{Z_i e^2}{|\mathbf{r}_i - \mathbf{R}_I|} + \frac{1}{2}\sum_{i\neq j}\frac{e^2}{|\mathbf{r}_i - \mathbf{r}_j|},$$
$$-\sum_I \frac{\hbar^2}{2M_I}\nabla_I^2 + \frac{1}{2}\sum_{I\neq J}\frac{Z_i Z_J e^2}{|\mathbf{R}_I - \mathbf{R}_J|} \tag{2.1}$$

The terms on the right-hand side of Eq. 2.1 represent, in order, the kinetic energy of electrons, Coulomb interactions between electrons and the nuclei, the Coulomb interactions between pairs of electrons, kinetic energy of nuclei, and Coulomb interactions between pairs of nuclei. The nuclear kinetic energy can be ignored, considering the mass M_I to be infinity, relative to that of electrons. This is called the *Born-Oppenheimer or adiabatic approximation.* Within this approximation, the nuclear dynamics does not cause electronic transitions, thus allowing the total wavefunction to be written as a product

of electronic and nuclear wavefunctions:

$$\Psi_s(\{\mathbf{r},\,\mathbf{R}\}) = \sum_i \chi_{si}(\mathbf{R})\Psi_i(\{\mathbf{r},\,\mathbf{R}\}); \quad \text{s = 1,2,3 ... are the states of coupled system}$$
(2.2)

where $\chi_{si}(\mathbf{R})$ are the nuclear wavefunctions, and $\Psi_i(\mathbf{r},\,\mathbf{R})$ defines a complete set of eigenfunctions for electrons at each $\{\mathbf{R}\}$.

For each electronic state i, the nuclear wavefunctions are determined by:

$$[-\sum_J \frac{\hbar^2}{2M_J}\nabla_J^2 + U_i(\{\mathbf{R}\}) - E_{ni}]\chi_{ni}(\{\mathbf{R}\}) = 0; \quad \text{n = 1,2,3... are the nuclear states}$$
(2.3)

and the many-body wavefunctions for the electrons, $\psi(\{\mathbf{r}_i\})$ are obtained by solving time-independent Schrödinger equation:

$$\hat{H}\Psi_i(\{\mathbf{r}_i\}) = E\Psi_i(\{\mathbf{r}_i\})$$
(2.4)

Here, the electronic hamiltonian is given as:

$$\hat{H} = \hat{T} + \hat{V}_{ext} + \hat{V}_{int} + E_{II}$$
(2.5)

with kinetic energy operator for electrons ($\hat{T}$), potential acting on electrons due to the nuclei (V_{ext}), and electron-electron interactions (V_{int}). The three terms can be written as:

$$\hat{T} = \sum_i -\frac{\hbar^2}{2m_e}\nabla_i^2, \quad \hat{V}_{ext} = \sum_{i,I} V_I(|\mathbf{r}_i - \mathbf{R}_I|), \quad \hat{V}_{int} = \frac{e^2}{2}\sum_{i\neq j}\frac{1}{|\mathbf{r}_i - \mathbf{r}_j|} \quad (2.6)$$

and E_{II} denotes the classical interactions of nuclei with one another.

The ground state wavefunction Ψ_o, the state with lowest energy, can be determined by minimizing the total energy with respect to all the parameters in $\Psi(\{\mathbf{r}_i\})$, with the constraint that Ψ must obey the particle symmetry and conservation laws. While all the other terms in Eq. 2.6 are exactly known in terms of Ψ, the exact value of electron-electron Coulomb interactions, V_{int} cannot be computed, and thus need to be approximated. Two independent-particle approaches, *non-interacting and Hartree-Fock*, assume that the electrons are uncorrelated, and approximate electron-electron interactions in two different ways. While the latter includes the interaction terms in the energy, the 'non-interacting' theories have some effective potential that incorporates some effect of real interaction, without an interaction term explicitly included in the effective hamiltonian. Density functional theory involves a non-interacting hamiltonian with an effective potential approximating the effects of exchange and correlation between electrons.

2.2   Density Functional Theory

Density functional theory is a theory of correlated many-body systems, having close associations with independent-particle methods. The works of Hohenberg-Kohn in 1964, and Kohn-Sham in 1965 have led to the formulations of DFT, which has now become the basis of present-day methods for treating electrons in atoms, molecules, and condensed matter.

2.2.1 Hohenberg-Kohn theorems

The two theorems proposed by Hohenberg and Kohn set the basis to formulate density functional theory as an exact theory of many-body systems.

Theorem I: For any system of interacting particle in an external potential $V_{ext}(\mathbf{r})$, the potential $V_{ext}(\mathbf{r})$ is determined uniquely by the ground state particle density, $n_o(\mathbf{r})$, except for a constant. Thus all properties of the system can be completely determined, once the ground state density $n_o(\mathbf{r})$ is known.

Theorem II: A universal functional for the energy E[n] in terms of the density $n(\mathbf{r})$ can be defined, for any external potential, $V_{ext}(\mathbf{r})$. For any particular $V_{ext}(\mathbf{r})$, the exact ground state energy of the system is the global minimum value of this functional, and the density $n(\mathbf{r})$ that minimizes the functional is the exact ground state density $n_o(\mathbf{r})$. The total energy functional, as uniquely determined by $n(\mathbf{r})$, is given by:

$$E_{HK}[n] = T[n] + \int d^3r V_{ext}(\mathbf{r})n(\mathbf{r}) + E_{int}[n] + E_{II} \qquad (2.7)$$

A functional $F_{HK}[n]$, which includes kinetic and potential energies of interacting electron system, can be defined as:

$$F_{HK}[n] = T[n] + E_{int}[n] \qquad (2.8)$$

Thus, if the functional $F_{HK}[n]$ is known, then by minimization of total energy with respect to $n(\mathbf{r})$, the exact ground state density and energy can be determined.

The operational difficulty in the above formulation is that there is no known way to extract kinetic energy directly from the density . When represented in terms of a set of N wavefunctions, the derivatives of kinetic energy as a function of number of electrons are discontinuous at integer occupation numbers. This implies that the exact functional will vary in a non-analytic manner as a function of number of electrons. This leads to Kohn-Sham approach, where kinetic energy is treated in terms of orbitals and interaction terms explicitly modeled as functionals of the density.

2.2.2   Kohn-Sham Ansatz

The approach proposed by Kohn and Sham for electronic structure calculations is to replace the original many-body problem by an auxilliary independent particle problem. The density of the original system is assumed to be equal to that of non-interacting system, and the interactins are incorporated into an exchange-correlation functional of the density. The auxiliary hamiltonian of the system has a kinetic operator and an effective local potential, $V_{eff}^{\sigma}(\mathbf{r})$ acting on an electron of spin σ at a point $\mathbf{r}$. The Kohn-Sham Schrödinger-like equations can be expressed as :

$$(H_{KS}^{\sigma} - \varepsilon_i^{\sigma})\psi_i^{\sigma}(\mathbf{r}) = 0 \tag{2.9}$$

where the ε_i are the eigenvalues, and H_{KS}^{σ} is the effective hamiltonian

$$\hat{H}_{KS}^{\sigma} = -\frac{1}{2}\nabla^2 + V_{KS}^{\sigma}(\mathbf{r}), \quad \text{using Hartree atomic units} \tag{2.10}$$

The expression for the ground state energy functional can be written as:

$$V_{KS} = V_{ext}(\mathbf{r}) + V_{Hartree}(\mathbf{r}) + V_{XC}(\mathbf{r}) \qquad (2.11)$$

where $E_{Hartree}$ is the self-interaction energy of density $n(\mathbf{r})$. The density of the system is given by:

$$n(\mathbf{r}) = \sum_{\sigma} \sum_{i=1}^{N^{\sigma}} |\psi_i^{\sigma}(\mathbf{r})|^2 \qquad (2.12)$$

and the kinetic energy T_s, as a functional of orbitals, is given by:

$$T_s = \frac{1}{2} \sum_{\sigma} \sum_{i=1}^{N^{\sigma}} \int d^3r |\psi_i^{\sigma}(\mathbf{r})|^2 \qquad (2.13)$$

The total electronic energy, E_{KS} given by:

$$E_{KS} = T_s[n] + \int d\mathbf{r} V_{ext}(\mathbf{r})n(\mathbf{r}) + \frac{1}{2} \int d^3\mathbf{r} d^3\mathbf{r}' \frac{n(\mathbf{r})n(\mathbf{r'})}{|\mathbf{r} - \mathbf{r'}|} + E_{II} + E_{XC}[n] \quad (2.14)$$

when minimized with respect to either the density $n(\mathbf{r})$, or the effective potential $V_{eff}^{\sigma}(\mathbf{r})$ leads to the ground state of the system. The only crucial ingredient that needs to be determined for obtaining the exact solution for the Kohn-Sham equations (Eq. 2.9-2.11) is the exchange-correlation functional E_{XC}, the approximations to which are discussed below.

2.2.3   Exchange-correlation functionals

In the Schrödinger equation, the motion of each electron is coupled to the motion of every other electron through Coulomb repulsions among them.

This repulsion lowers the electrostatic energy, and the energy reduction is termed as the exchange-correlation energy of the system. The exchange-correlation potential, V_{XC} in the effective hamiltonian (Eq. 2.10) is given by:

$$V_{XC} = \frac{\delta E_{XC}}{\delta n(\vec{\mathbf{r}})} \tag{2.15}$$

Hence, the accurate approximations of E_{XC} are necessary to obtain ground state energy and density. Kohn and Sham proposed a non-emperical approximation using exchange-correlation energy per electron, $\varepsilon_{xc}^{uniform}(n)$ of an electron gas of uniform density n. This is called *'local density approximation'*. The real system with nonuniform density is assumed to locally consist of infinitesimal volume elements, each with a uniform electron density. This leads to the following relation for E_{XC}:

$$E_{XC}^{LDA}[n] = \int d^3r n(\vec{r}) \varepsilon_{xc}^{uniform}(n(\vec{r})) \tag{2.16}$$

This approximation is exact for uniform density and correct and accuarate for systems with spatially-varying density.

To make these functionals more accurate, the idea of exchange-correlation energy in terms of density, $n(\vec{r})$, can be extended to include additional exact constraints into the approximations. Adding a second element, the gradient of density, gives rise to *'generalized gradient approximation (GGA)'* of the exchange-correlation functional, which is expressed as:

$$E_{XC}^{approx}[n] = \int d^3r n(\vec{r}) \varepsilon_{xc}^{approx}(n(\vec{r}), \nabla n(\vec{r})) \tag{2.17}$$

2.2.4   Solving Kohn-Sham equations

The set of Schrödinger-like one-electron equations i.e. Eqs 2.9-2.11, need to be solved such that the $V_{eff}(\mathbf{r})$ and density $n(\mathbf{r})$ are consistent. The steps involved in solving these equations to acheive self-consistency are as under:

1. Consider a trial electron density, $n(\mathbf{r})$.

2. Calculate $V_{eff}(\mathbf{r})$ using Eq. 2.11.

3. Solve for electron wavefunctions (Eq. 2.9 and 2.10).

4. Calculate a new electron density using Eq. 2.12.

5. Check for the convergence of $n(\mathbf{r})$. If achieved, calculate total energy E_{KS} (Eq. 2.14), forces, stresses, and eigenvalues, otherwise reiterate the calculations from Step 2.

2.3   Force and stress from electronic structure

2.3.1   Force theorem

The force theorem, derived by Feynman in 1939, states that the force on the nucleus is strictly in terms of the charge density, independent of the electron kinetic energy, exchange, and correlation. In electronic structure theory, this is termed as "Hellmann-Feynman theorem". The force $\mathbf{F}_I$ acting on a nucleus $\mathbf{R}_I$ is given as:

$$\mathbf{F}_I = -\frac{\partial E}{\partial \mathbf{R}_I} = -\int d^3 r n(\mathbf{r}) \frac{\partial V_{ext}(\mathbf{r})}{\partial \mathbf{R}_I} - \frac{\partial E_{II}}{\partial \mathbf{R}_I} \qquad (2.18)$$

It is important to note that Eq. 2.18 follows if the electron density is held constant to first order as the nucleus moves.

2.3.2 Stress calculations

In the condensed matter, the state of a system is specified by the forces on each atom and the stress. The forces that act upon (or through) the surface of the element, due to the surrounding material contribute to the stresses transmitted throughout the volume of the element. Strain is deformation of a material that causes a displacement $\mathbf{u}$ of a point $\mathbf{r}_i \rightarrow \mathbf{r'}_i$, as a function of the coordinate $\mathbf{r}$. The strain tensor $u_\alpha\beta$, can be defined as:

$$u_{\alpha\beta} = \frac{1}{2}(\frac{\partial u_\alpha}{\partial r_\beta} + \frac{\partial u_\beta}{\partial r_\alpha}) \qquad (2.19)$$

over cartesian indices, α,β. In quantum mechanics, if a system is in equilibrium and the strain is homogeneous over macroscopic regions, the macroscopic average stress tensor $\sigma_{\alpha\beta}$ is defined in terms of energy and strain tensor $\epsilon_{\alpha\beta}$ per unit volume as:

$$\sigma_{\alpha\beta} = -\frac{1}{\Omega}\frac{\partial E}{\partial \epsilon_{\alpha\beta}} \qquad (2.20)$$

The stress-strain relations describe elastic phenomena in materials. For example, the elastic constants are given by:

$$C_{\alpha\beta;\gamma\delta} = \frac{1}{\Omega}\frac{\partial^2 E_{total}}{\partial u_{\alpha\beta}\partial u_{\gamma\delta}} = -\frac{\partial \sigma_{\alpha\beta}}{\partial u_{\gamma\delta}} \qquad (2.21)$$

Further, the above definition of stress (Eq. 2.20) with the assumption of homogeneous strains holds good when the energy of the system be minimum

with respect to all internal degrees of freedom. But for the calculation of actual stress in real materials, one must impose an additional requirement that the force on each nucleus vanishes, $\mathbf{F}_I = 0$, in presence of the strain. The displacement at which this condition is satisfied is defined as:

$$\mathbf{u}_{s,\alpha} = \sum_\beta \epsilon_{\alpha\beta} \tau_{s,\beta} + \mathbf{u}_{s,\alpha}^{int} \qquad (2.22)$$

The first term represents uniform scaling of space, $\mathbf{r}_\alpha \to (\delta_{\alpha\beta} + \epsilon_{\alpha\beta})\mathbf{r}_\beta$, $\mathbf{r}$ being any vector in space. The second term shows the deviations, or "internal strains", which are crucial for understanding stress-strain curves in low-symmetry systems. The calculation of these internal strains is one of the key areas where theory adds information to the theory of elasticity, given the difficulty in resolving the atomic positions in a strained systems through experiments.

2.4   Pseudopotentials

The idea behind construction of pseudopotentials is to replace the strong Coulomb potential of the nucleus and the effect of tightly bound core electrons by an effective ionic potential acting on the valence electrons. The aim of pseudopotential theory is to find effective potentials that represent the scattering over the desired energy range. Most present-day electronic calculations are based on 'ab initio norm-conserving pseudopotentials' and 'ultrasoft pseudopotentials'.

2.4.1 Norm-conserving pseudopotentials (NCPPs)

The norm-conserving pseudofunctions ψ^{PS} are normalized and are solutions of model potential chosen to reproduce the valence properties of an all-electron calculations. The orthogonality condition:

$$\langle \psi_i^{\sigma,PS} | \psi_j^{\sigma',PS} \rangle = \delta_{i,j} \delta_{\sigma,\sigma'} \tag{2.23}$$

needs to be satisfied so that the Kohn-Sham equations has the same form:

$$(H_{KS}^{\sigma,PS} - \varepsilon_i^\sigma) \psi_i^{\sigma,PS}(\mathbf{r}) = 0 \tag{2.24}$$

To be defined as a good *ab initio* pseudopotential, it is required that the NCPP equals the atomic potential outside the "core region" of radius R_c, the logarithmic derivatives of the all-electron and pseudo wavefunctions agree at R_c, the first energy derivative of the logarithmic derivatives of the pseudo- and 'real' wave functions agree at R_c, and the norm-conservation condition is satisfied.

2.4.2 Ultrasoft pseudopotentials

Ultrsoft pseudopotentials accurately calculate the effective potential by a transformation that re-defines the problem in terms of a smooth function, and an auxilliary function around each ion core that represents the rapidly varying part of the density. The condition of norm-conservation is relaxed. Thus, the critical radius R_c much larger than for the norm-conserving pseudopotential can be chosen, while maintaining the desired accuracy.

2.5   Calculation of Phonons

Vibrational spectra provide wealth of information about the lattice-dynamical behavior of solids. Accurate information on the force constants, static dielectric constants, piezoelectric constants, electron-phonon interactions etc. can be provided by theory of phonons, which is ultimately a part of electronic structure. The total energy, within Born-Oppenheimer approximation, can be viewed as a function of the positions of the nuclei $E(\{\mathbf{R}_i\})$. The two approaches in the calculation of phonons using first-principles theory are:

(1) Direct calculation of total energy as a function of the positions of the atoms (frozen phonon method)

(2) Perturbative approach involving calculations of the derivative of energy (response function method)

2.5.1   Frozen phonons

In frozen phonon method, a small, but finite perturbation is frozen in the system, and the total energy and forces are calculated with nuclei "frozen" at positions $\{\mathbf{R}_I\}$. The forces on atoms can be calculated within the framework of density functional theory, which makes it a direct approach for phonon calculations. Then, the force constant matrix elements defined by numerical dervatives of displacements as calculated as :

$$C_{I,\alpha;J,\beta} \approx -\frac{\Delta F_{I,\alpha}}{\Delta \mathbf{R}_{J,\beta}} \tag{2.25}$$

and dynamical matrix $\tilde{D}_{I,\alpha;J,\beta}$ is computed from the force constant matrix as:

$$\tilde{D}_{I,\alpha;J,\beta} = C_{I,\alpha;J,\beta} \frac{1}{\sqrt{M_I M_J}} \tag{2.26}$$

Phonon frequencies and eigenvectors are obtained by digonalization of the dynamical matrix. However, this technique determines phonon dispersion curves for a crystal only with large "supercell" calculations, whose size depends on commensurability of perturbation, hence increasing the computational cost of phonon calculations at lower $\mathbf{q}$-points.

2.5.2 Density Functional Perturbation Theory

Perturbative theory involves systematic expansion of hamiltonian $\hat{H}^o + \lambda \Delta \hat{H}$ in the powers of the perturbation. The first order expressions depending on unperturbed wavefunctions and $\Delta \hat{H}$ to the first-order are given as the 'generalized force' on an atom. To obtain the interatomic force constants (IFCs), we needs to compute second derivatives of ground state energy with respect to the perturbation i.e. nuclear displacements, which can be calculated using efficient electronic structure methods. This is given by:

$$\frac{\partial^2 E(\{\mathbf{R}\})}{\partial \mathbf{R}_I \partial \mathbf{R}_J} = \int \frac{\partial n(\mathbf{r})}{\partial \mathbf{R}_J} \frac{\partial V_{[R]}(\mathbf{r})}{\partial \mathbf{R}_I} d\mathbf{r} + \delta_{IJ} \int n(fr) \frac{\partial^2 V_{[\mathbf{R}]}(\mathbf{r})}{\partial \mathbf{R}_I \partial \mathbf{R}_J} d\mathbf{r} + \frac{\partial^2 E_N(\{\mathbf{R}\})}{\partial \mathbf{R}_I \partial \mathbf{R}_J} \tag{2.27}$$

The linear response of the charge density with respect to atomic positions can be calculated as:

$$\frac{\partial n(\mathbf{r})}{\partial \mathbf{R}_I} = 4Re \sum_{n=1}^{N/2} \psi_n^*(\mathbf{r}) \frac{\partial \psi_n(\mathbf{r})}{\partial \mathbf{R}_I} \tag{2.28}$$

The derivatives of KS orbitals, $\frac{\partial \psi_n(\mathbf{r})}{\partial \mathbf{R}_I}$ are calculated as:

$$(H_{SCF} - \epsilon_n)\frac{\partial \psi_n(\mathbf{r})}{\partial \mathbf{R}_I} = -\left(\frac{\partial V_{SCF}(\mathbf{r})}{\partial \mathbf{R}_I} - \frac{\partial \epsilon_n}{\partial \mathbf{R}_I}\right)\psi_n(\mathbf{r}) \qquad (2.29)$$

with first-order derivative of self-consistent potential given as:

$$\frac{\partial V_{SCF}(\mathbf{r})}{\partial \mathbf{R}_I} = \frac{\partial V_{[\mathbf{R}]}(\mathbf{r})}{\partial \mathbf{R}_I} + e^2 \int \frac{1}{|\mathbf{r}-\mathbf{r}'|}\frac{\partial n(\mathbf{r}')}{\partial \mathbf{R}_I}d\mathbf{r}' + \int \frac{\delta v_{xc}(\mathbf{r})}{\delta n(\mathbf{r}')}\frac{\partial n(\mathbf{r}')}{\partial \mathbf{R}_I}d\mathbf{r}' \quad (2.30)$$

and first-order derivative of the KS eigenvalue, ϵ_n, expressed as:

$$\frac{\partial \epsilon_n}{\partial \mathbf{R}_I} = \langle \psi_n|\frac{\partial V_{SCF}}{\partial \mathbf{R}_I}|\psi_n\rangle \qquad (2.31)$$

The Eqs. (2.28-2.30) form a set of self-consistent set of equations for cal-culation of response to an external perturbation, V_{ext}. The solution of the linear system can be obtained by employing efficient iterative techniques such as conjugate gradients or the steepest descents. These calculations can be carried out for obtaining phonon dispersion curves for any material, and show nearly perfect agreement with experiments. Other information derived from the phonon calculations includes phonon density of states and electron-phonon coupling.

Chapter 3

Deformation induced polymorphism in HCP metals: First-principles analysis

3.1 Introduction

In recent years, investigation of deformation mechanisms in single crystals of micrometer dimensions has been the focus of attention of numerous experimental studies [4, 5, 11–14]. The phenomenon of plastic flow is particularly intriguing in hexagonal-close-packed metals, because of fewer number of available slip systems at room temperature than in BCC and FCC metals. Deformation twinning is known to be the key mode of deformation in HCP metals with sample sizes in micrometer i.e. d $\geq 1.0\mu$m [4, 15]. As the sample size is lowered to submicron length i.e. d $\leq 1.0\mu$m, the slip-mediated deformation is a prominent mechanism with strong crystal size effects on the

flow stress and dislocation behaviors. A recent study by Yu *et al.* [5] revealed a controlled plastic flow in the presence of very high stresses in the necked region of a Ti-5 at.% Al alloy. Their HRTEM study showed an increase in the basal stacking faults confirming the effect of sample size on the transition of deformation mode from twinning to ordinary dislocation plasticity (ODP) and the likelihood of cross-slip in HCP metals.

First-principles quantum-mechanical methods are increasingly used in material-specific exploration of deformation anisotropy in materials [16, 17]. The efficacy of theoretical studies is particularly advantageous over experiments where the stresses developed in the system result in differential strains in atomic layers, in addition to the homogeneous strain [18]. Additionally, the results show excellent agreement with the experiments on small-volume single-crystal samples, because of (a) lower concentration of imperfections prior to loading, and (b) experimental stress levels approaching the ideal strength of the material [14, 19]. This provides an impetus for the theoretical study of planar faults in hexagonal-closed-packed metals at the atomic scale to understand their underlying deformation behavior. Exceptionally superior high specific strength of Titanium, showing dislocation-mediated plastic flow in submicron-sized samples, has led us to focus on the energetics of stacking faults and local structural transformations accompanying these faults.

As a model system of the present investigation, we choose the basal (0001) plane of α-Titanium. We present a remarkable finding of the existence of

deformation-induced polymorphs of Ti, stabilized by strain-mediated inter-actions between stacking faults on the basal plane. The relevance of $\frac{c}{a}$ ratio in determining the nature of slip phenomenon in HCP metals has guided our search for similar polymorphs in other HCP metals. A Landau-theoretical desription of structural signatures of titanium polymorphs in terms of homo-geneous and inhomogeneous strain is presented to develop an understanding of these polymorphs, in reference to HCP structure of titanium.

3.2   Computational Details

Our calculations are based on first-principles density functional theory (DFT) and plane-wave pseudopotential method as implemented in Quantum ESPRESSO [20] (QE). The ionic core-valence electron interactions are represented with ultrasoft pseudopotentials [21] and electronic exchange-correlation energy is approximated with a generalized gradient approximation (GGA) as parametrized by Perdew-Wang [22] for titanium, Perdew-Burke-Ernzerhof [23] for beryl-lium, yttrium, and lanthanum, and with a local density approximation (LDA) as parametrized by Perdew-Zunger [24] for magnesium and zinc. The choice of these functionals is based on the availability of reliable pseudopotentials with QE, and physical results do not depend on them. Kohn-Sham wave functions are expanded in a plane-wave basis set truncated with energy cut-off of 30 Ry (and a corresponding cutoff of 240 Ry for charge density). In-tegrations over Brillouin Zone (BZ) are sampled with a uniform (20x20x12) k-grid for the bulk hcp structures, and the atomic structures are relaxed us-ing Broyden, Fetcher, Goldfarb, Shanno (BFGS)-based algorithm until the

Hellman-Feynman forces on each atom are lower than 0.001 Ry/bohr. Supercells with six unit cells of HCP structure stacked along the c-axis are used in generating planar faults on the basal (0001) plane, and atomic and cell relaxations are carried out to equilibrate the structures with respect to all the degrees of freedom. Energies of the new structures of Ti relative to that of HCP Ti are confirmed using ABINIT [25] implementation of DFT with a norm-conserving pseudopotential, [26] and a local density approximation to exchange-correlation energy functionals as parameterized by Perdew-Wang [27].

Dynamical matrices and phonon frequencies of Ti polymorphs are obtained using the DFT linear response [28] method (Quantum ESPRESSO implementation), at $\mathbf{q}$-points on a uniform (2x2x1) mesh in the BZ. Assuming a weak dependence of phonon frequencies on the changes in volume as a function of temperature (justified by a small thermal expansion coefficient), vibrational contribution to free energy is estimated within a harmonic approximation [29, 30] given by

$$F_{vib} = E_{total} + \frac{k_B T}{N_q} \sum_{q,i} \log \left[2 \sinh \left(\frac{\hbar w_{iq}}{2 k_B T} \right) \right] \tag{3.1}$$

where N_q is the number of $\mathbf{q}$-points on (20x20x12) mesh in the BZ, and ω_{iq} is the frequency of ith normal mode at wavevector $\mathbf{q}$, obtained using Fourier interpolation of dynamical matrices at the (2x2x1) mesh of q-points computed with DFT linear response.

3.3   Results and Discussions

3.3.1   Study of faults on (0001) plane of titanium

The extent of deformation on a crsytallographic plane is determined by the generalized stacking fault vector $\vec{\mathbf{f}}$, given by $\vec{\mathbf{f}} = x\vec{a_1} + y\vec{a_2}$, where $\vec{a_1}$, $\vec{a_2}$ are cell vectors of the plane, and $(x \leq 1, y \leq 1)$ are fractional displacements. An example of a fault with $\vec{\mathbf{f}} = \frac{1}{2}\vec{a_1} + \frac{1}{3}\vec{a_2}$ on the basal (0001) of a supercell of Ti is shown in Fig. 3.1. The energetics of faults in crystals are studied by ob-

Shear deformation

HCP Titanium   **Faulted configuration**
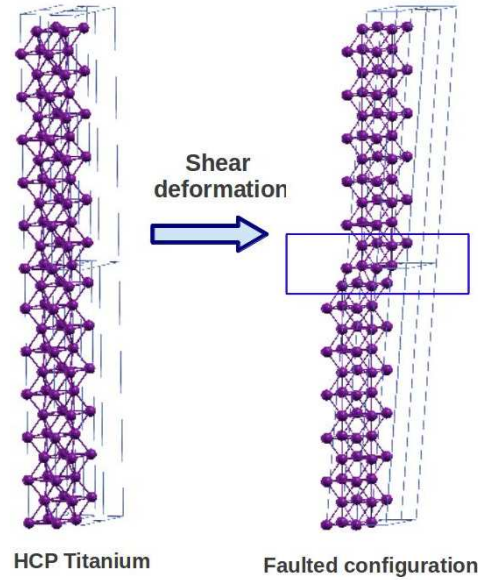
Figure 3.1: Faulted configuration with $\vec{\mathbf{f}} = \frac{1}{2}\vec{a_1} + \frac{1}{3}\vec{a_2}$ on the basal (0001) plane of titanium

taining a generalized stacking fault energy surface (or the γ-surface), which represents the energy cost of displacing one semi-infinite block of the crystal relative to the other as a function of a fault vector $\vec{\mathbf{f}}$ in a plane (Vitek, 1968). The fault energies on the basal plane of titanium are calculated with (x, y) on a uniform (6x6) mesh, and then Fourier interpolated to obtain energy of

a fault of an arbitarary vector $\vec{\mathbf{f}}$ (see Fig. 3.2a).
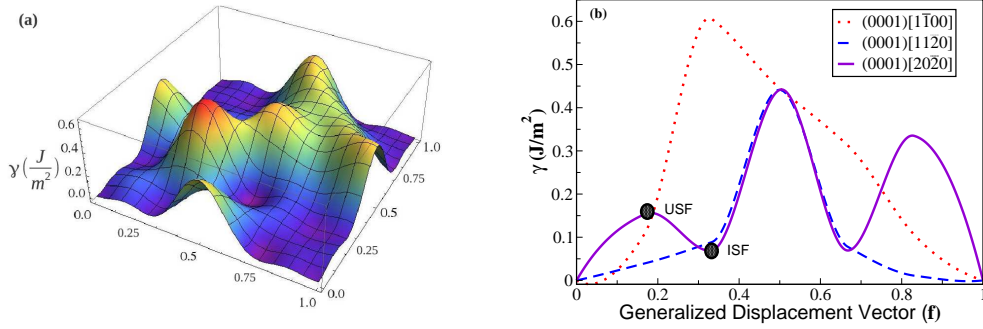
Figure 3.2: Fault energetics on basal (0001) plane of titanium: (a) γ-surface, (b) Generalized stacking fault energy curves

A few special points on the γ-surface provide insight into the energetics of dislocation nucleation and mobility on a plane, highlighting plastic deformation anisotropy in a material. The local minimum in the γ-surface gives the intrinsic stacking fault (ISF) energy, which is an indirect measure of the width of stacking fault on that particular plane. The configuration of minimum energy barrier (a saddle point) required for a dislocation partial to nucleate is the unstable stacking fault (USF).

The generalized stacking fault energy curves (Fig. 3.2b) extracted as sections of the γ-surface on the basal plane of Ti exhibit highly directional nature of the slip. The energy of an FCC fault along the $(0001)[1\bar{1}00]$ slip system of Ti is 315 mJ/m^2 (12.23 meV/atom) which corresponds well with the experimental value of 310 mJ/m^2 [31]. Our calculations also show a local minimum along $[20\bar{2}0]$ with a significantly low energy of 69 mJ/m^2, and an energy barrier of 153 mJ/m^2 along the same direction. We refer to

these configurations as the ISF and USF configurations, respectively on the $(0001)[20\bar{2}0]$ slip system of titanium.

3.3.2   Strain-mediated interactions of planar faults

Finding relatively high energy barriers, we optimized the faulted structures with respect to all the degrees of freedom through full (concurrent atomic and cell) relaxations. Because of the small (nano-scale) supercell, with c $= 6c_o \approx 2.7$nm, the strain-mediated interactions propagate to the adjacent planar faults, leading to the changes in cell vectors. Thus, it is not possible to define a definite fault vector $\vec{\mathbf{f}}$ of the final relaxed structure, and correspond a GSF energy ($\phi\vec{\mathbf{f}}$). If the size of the supercell were large (c $\rightarrow \infty$), the cell-relaxation should not change the displacement vector of slip, and hence the γ-surface. The exception to this size-dependent behavior occurs in the case of FCC stacking fault configuration in HCP Ti. The fault vector is essentially unchanged i.e. $\vec{\mathbf{f}} = \frac{2}{3}\vec{a_1} + \frac{2}{3}\vec{a_2}$, and the atomic layers away from the fault show negligible displacements, indicating the formation of a shear step with no deformation in the cell volume (see Fig. 6.1).

Surprisingly, such variable-cell relaxation of nano-scaled structures has revealed three inequivalent structures with energies comparable to that of pristine HCP titanium (see Table 5.1)! The morphology of these structures show sliding in all the atomic planes, thus exhibiting no structural similarities with the localized nature of stacking faults in crystals (Fig. 6.1). To
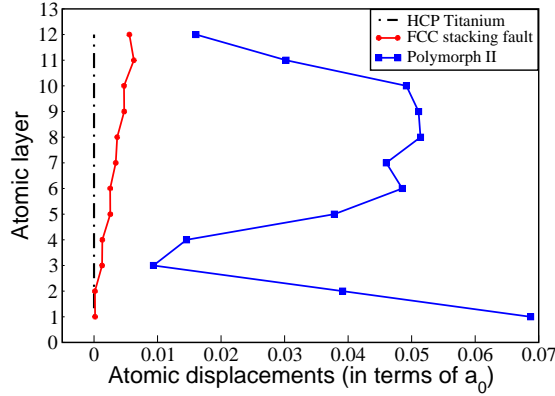
Figure 3.3: Atomic displacements ($d_n^{faulted} = |\vec{r}_n|^{faulted} - |\vec{r}_n|^{ideal}$) in faulted configurations on cell-relaxation

Table 3.1: Energies and structural parameters of new structures using QE with reference to HCP titanium

	ΔE	c-vector (in units of a_o)		
	(meV/atom)	c_x	c_x	c_z
HCP Ti	0	0.0	0.0	9.478
Structure I	0.78	0.834	0.0	9.499
Structure II	1.06	0.916	0.001	9.492
Structure III	1.15	0.501	0.685	9.499

develop further credibility in these unexpected results, we carried out structural relaxations using ABINIT [25] with these three structures as the initial guess. The final relaxed structures are indeed the same as those obtained using QE, within the typical DFT errors, and have energies essentially the same as that of pristine HCP titanium (Table 3.2). Henceforth, we call these novel structures as the 'deformation-induced polymorphs' of titanium.

In comparison with the pristine HCP titanium, the estimated bulk moduli, surface energies (Table 3.3), and the electronic density of states (e-DoS) (see Fig. 3.4) of the polymorphs are nearly the same. The density of states at the

Table 3.2: Energies and structural parameters of new structures using ABINIT with reference to HCP titanium

	ΔE	c-vector (in units of a_o)		
	(meV/atom)	c_x	c_x	c_z
HCP Ti	0	0.0	0.0	9.494
Structure I	0.074	0.828	0.0	9.522
Structure II	0.073	0.912	0.00	9.514
Structure III	0.074	0.498	0.679	9.523

Fermi energy increases in polymorph III, but is nearly unchanged in polymorph I and II, with respect to HCP titanium. The coordination number of each atom in the three polymorphs remains 12, indicating the preservation of the local structural coordination.

Further, we use the distributions of bond lengths, D($\mathbf{b}$), to highlight important structural differences amongst the polymorphs (Fig. 3.5). The $\frac{c}{a}$ ratio of titanium ($\sim$1.582) deviates from the ideal value for HCP structure (1.633), which results in different in-plane and out-of-plane bond lengths. Thus, D($\mathbf{b}$) of the HCP titanium contains two peaks (δ-functions), A and B, at 2.87 $\overset{\circ}{A}$ and 2.93 $\overset{\circ}{A}$, corresponding to out-of-plane and in-plane bond lengths respectively, as a reflection of a non-ideal $\frac{c}{a}$ ratio. The D($\mathbf{b}$) functions of the titanium polymorphs exhibit significant changes in the out-of-plane bond lengths (Fig. 3.5), suggesting a link between the $\frac{c}{a}$ ratio of titanium and the structural features of these polymorphs.
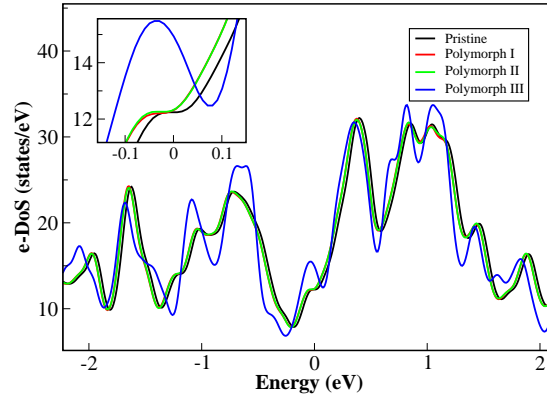
Figure 3.4: Electronic DoS of Ti structures: HCP and polymorphs

Table 3.3: Bulk properties of Ti polymorphs

	Surface Energy (J/m^2)	Bulk Modulus (GPa)
Pristine Ti	1.93	117
Polymorph I	1.92	116
Polymorph II	1.92	116
Polymorph III	1.93	115
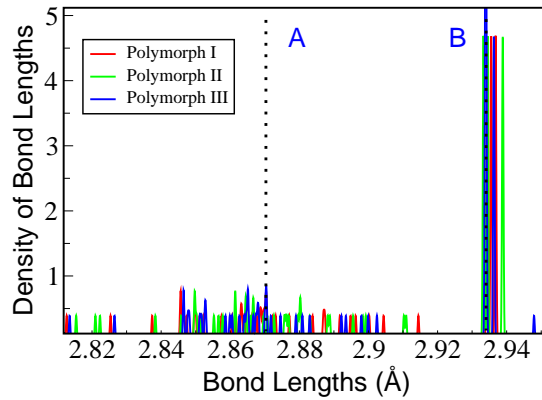
Figure 3.5: Bond length distribution in titanium polymorphs. A and B peaks correspond to out-of-plane and in-plane bond lengths respectively

3.3.3 Generality of existence of polymorphs in HCP metals

To probe the generality of these results, and establish possible existence of these polymorphs in other HCP metals viz. yttrium, beryllium, lanthanum, magnesium, and zinc, we obtained the minimum-energy structure of polymorph II of each of these metals, and identified the structural features that correlate with their $\frac{c}{a}$ ratio. In each of these metals, the atomic structure of polymorph II is generated by shear deformation along the basal plane, with fault vectors analogous to that of polymorph II of titanium, and structural optimization with respect to all the degrees of freedom is carried out, resulting in an energy minimum. We then estimate the energy of polymorph II, relative to that of the HCP structure, for each of of these metals. Our results strikingly reveal the existence of energetically stable deformation-induced polymorphs in HCP metals, except for zinc probably due to its unsually high $\frac{c}{a}$ ratio (Table 3.4).

The local changes in the atomic structure of the polymorph II for each of these HCP metals are summarized in Table 3.5, classifying the differences in terms of $\frac{c}{a}$ ratio and the valence orbitals involved in bonding. Interestingly, the new structure of zinc shows significant structural transformation with reference to the HCP structure (see Table 3.5), changing the overall $\frac{c}{a}$ ratio towards its ideal value, with an energy cost of $\sim$1.86 meV/atom. Such relatively higher energies reflect a weaker tendency of polymorphism in zinc, in contrast to that in the other HCP metals.

Table 3.4: Energies of polymorph II of HCP metals

HCP metal	$\frac{c}{a}$ value	Energy Difference (ΔE) (meV/atom)
Y	1.55	0.1
Be	1.57	0.28
Ti	1.58	1.0
Mg	1.62	0.5
La	1.61	0.46
Zn	1.87	1.86

Table 3.5: Trends in bond length distributions in polymorph II of HCP metals and correlation with $\frac{c}{a}$ ratio and valence orbitals

|	s, p orbitals	d orbitals
	Negligible changes in the in-plane bond lengths	
$\frac{c}{a}$ <1.633	**Be**: Insignificant change in the out-of-plane bond lengths,	**Y** and **Ti**: contraction and expansion in out-of-plane bond lengths
	Mg: Out-of-plane bond lengths approaching the in-plane bond lengths	**La**: Significant spread in the out-of-plane bond lengths
$\frac{c}{a}$ >1.633	_	**Zn**: increase in in-plane bond lengths, decrease in out-of-plane bond lengths, $\frac{c}{a}$ ratio approaching the ideal value
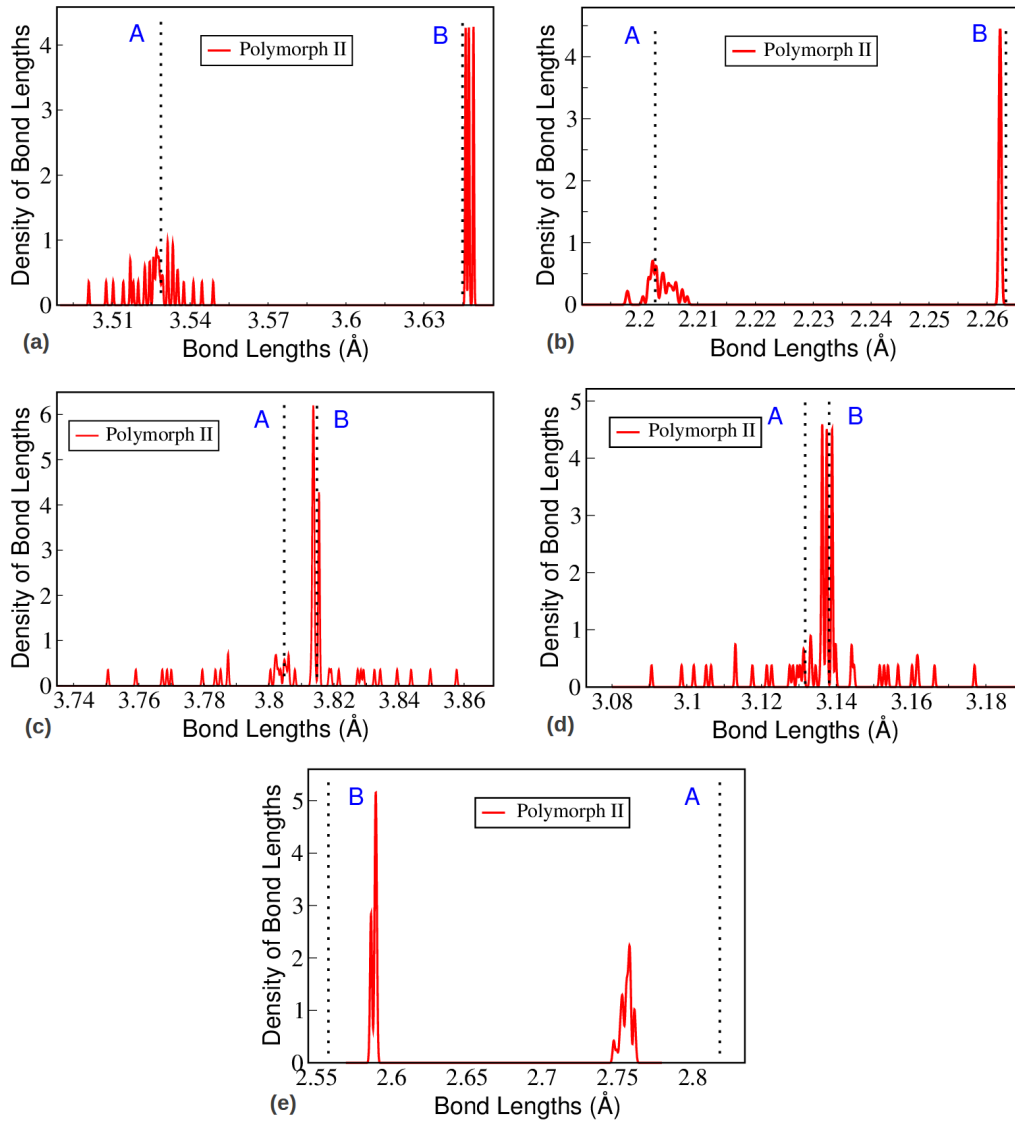
Figure 3.6: Bond length distributions in polymorph II of HCP metals: (a) yttrium, (b) beryllium, (c) lanthanum, (d) magnesium, and (e) zinc. A and B peaks correspond to out-of-plane and in-plane bond lengths respectively

3.3.4 Temperture-dependent stability of polymorphs of titanium

In light of the technological relevance of titanium in structural applications, we now focus on the analysis of three of its polymorphs. Negligible difference in energies of these polymorphs relative to that of HCP titanium prompts the evaluation of their structural stability as a function of temperature. Vibrational spectra of the three polymorphs confirm their local structural stability (Fig. 3.8), and bear the signature of spread in the out-of-plane bond lengths in the frequencies at the wavevector $(0,0,\frac{1}{2})$ i.e. A-point of the Brillouin zone. The three optical phonon modes (doubly degenerate modes of in-plane displacements, and a third mode of out-of-plane displacements) at the Γ-point in the unit cell of HCP titanium (Fig. 3.7) are correlated with the eigenvectors of the normal modes in the polymorphs, by calculating a correlation matrix as

$$S_{\mu\nu} = \langle e_\mu | e'_\nu \rangle, \tag{3.2}$$

where e_μ is the eigenvector of μth mode of HCP titanium, and e'$_\nu$ is the eigenvector of νth mode of a polymorph, both determined for the 12-atom supercells.

Analysis of the normal modes with maximum overlap with the normal modes of HCP titanium shows softening of the modes corresponding to the in-plane atomic displacements, and hardening of the modes representing out-of-plane atomic displacements (Table 5). This can be readily understood from the
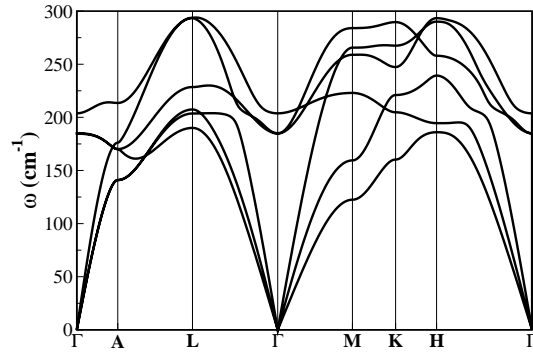
Figure 3.7: Vibrational Spectrum for bulk Ti
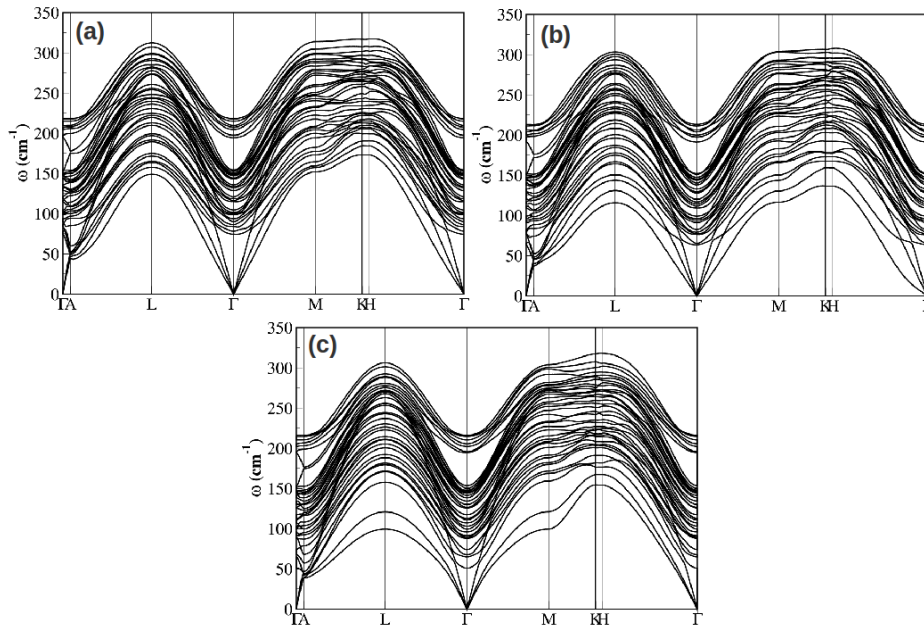
Figure 3.8: Vibrational spectra for (a) polymorph I, (b) polymorph II, and (c) polymorph III

slight increase in the in-plane bond lengths of all the polymorphs, and a decrease in the out-of-plane bond lengths in polymorph III, evident from D(**b**) of titanium structures (see Fig. 3.5). Note the hardest optical mode of polymorph III. Furthermore, the elastic constants obtained through a long wavelength limit ($q \rightarrow 0$) of transverse acoustic phonons along the ΓA- segment

Table 3.6: In-plane and out-of-plane frequencies (in cm^{-1}) at Γ-point

Frequency (in cm^{-1})			
	In-plane		Out-of-plane
	Mode I	Mode II	Mode III
Pristine HCP	184	185	204
Polymorph I	150	154	210
Polymorph II	148	152	211
Polymorph III	147	147	216

seem to be lower for all the polymorphs, indicating an increased tendency of strains along c-direction in the polymorphs.
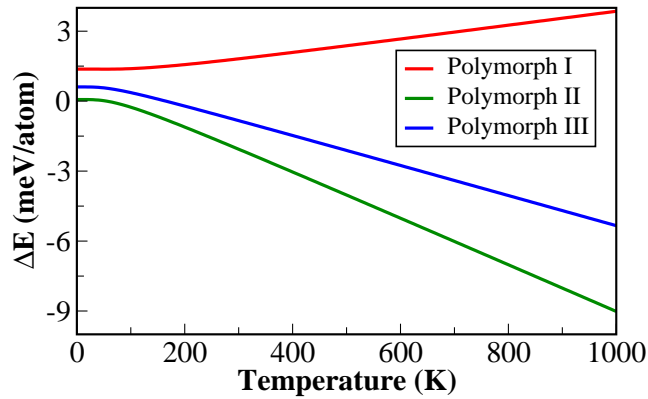
Figure 3.9: Vibrational contributions to free energies of polymorphs relative to HCP structure

Temperature-dependent vibrational free energies of the polymorphs relative to the HCP structure (Fig. 3.9), obtained within a harmonic approximation, reveal a monotonous increase in free energy of polymorph I, rendering it relatively less stable as T increases. This is in contrast to polymorph II and III, whose vibrational free energies tend to increase their stabilty with an increase in temperature from 0 to 1000 K.

3.3.5   Structural Analysis

We now establish a Landau theoretical picture of the polymorphs that con-
cisely describes their structures as a distortion of the reference HCP titanium.
The structures of these polymorphs arise from a combination of (a) localized
slip (at $\vec{c} = 6c_o$, in the present study), originating from the initial slip $\vec{f}$ on the
basal plane, (b) average displacements of A and B sublattice sites in each
of the primitive cells, spatial variations of which give the inhomogeneous
strain, and (c) internal strains associated with inter-sublattice displacements
of atomic planes A and B. Homogeneous strain in the cell, ϵ_{xz}, is obtained
in the elastic regime as:

$$\epsilon_{xz} = \frac{c_x}{6c_0} \qquad (3.3)$$

c_x and c_o being the x-component and z-component of c-vector of polymorph
and HCP titanium respectively. In polymorph III, the strain has both xz-
and yz- components, and this is appropriately generalized (see Table 6).

To separate the inhomogeneous deformation into acoustic phonons (inhomo-
geneous strain) and optical phonons (internal strain), we define two degrees
of freedom for each unit cell, i (i = 1 to 6, in the present study):

$$a_i = \frac{u_{Ai} + u_{Bi}}{2} \qquad (3.4)$$

$$o_i = \frac{u_{Ai} - u_{Bi}}{2} \qquad (3.5)$$

where u is the x-component of atomic displacement. The a_i describes the
average displacement of adjacent A and B atomic planes relative to that in the

HCP structure, and o_i describes the relative displacements of adjacent A and B atomic planes in a polymorph. To compute a_i and o_i, we first filter out the contributions of homogeneous strain on the atomic positions (using relation 3.3). This is done by representing atomic positions in a polymorph in reduced (crystal) coordinates, and obtaining $u_n^p = d_n^p$-d_n^o, d_n^p and d_n^o being the atomic positions in crystal coordinates of n atoms (n = 1 to 12, in the present study) in a polymorph and HCP structure respectively. The $a_i^{(s)}$ obtained using Equation 3.4, represent a displacement field of the inhomogeneous strains in the system, and contain linear and periodic components of the atomic displacements (see Fig. 3.10).

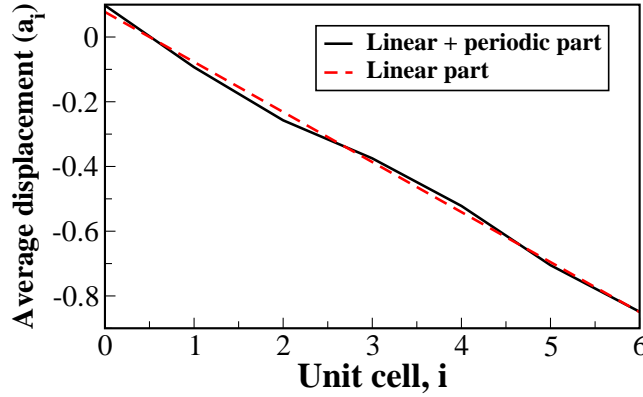Figure 3.10: Displacement field of acoustic phonons (inhomogeneous strain)

We further isolate the linear part of atomic displacements by using,

$$\widetilde{a}_i = a_i - i * (\epsilon'_{xz})(c_o) - \bar{a} \tag{3.6}$$

where ϵ'_{xz} is responsible for the linear part of the $a_i^{(s)}$, and $\bar{a}$ is the average of $a_i^{(s)}$. It is important to note that the slope of linear part of $a_i^{(s)}$ is negative

(Table 6), signifying that ϵ'_{xz} partly compensates the homogeneous deformation (Eq. 3.3), thus imparting structural stability to the polymorphs. $\widetilde{a}_i^{(s)}$ are periodic after 12-atomic planes, and show distinct inhomogeneous strain patterns for each of the three polymorphs (see Fig. 3.11a). These $\widetilde{a}_i^{(s)}$, when
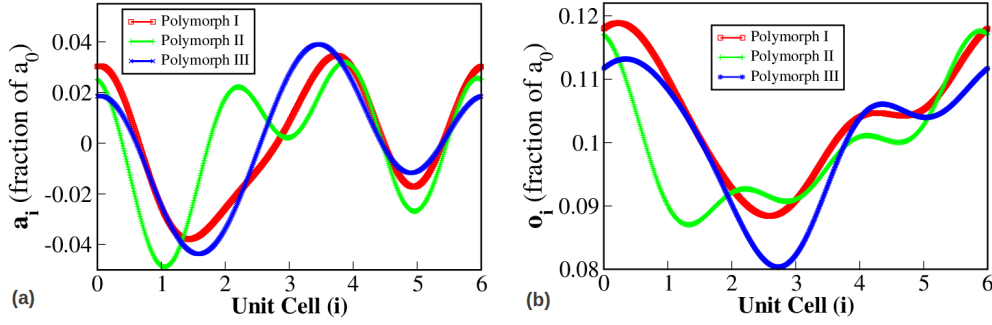
Figure 3.11: Inhomogeneous displacements in Ti polymorphs

represented in Fourier space (Fig. 3.12a), indicate relative weights of the acoustic phonons of different wavevectors (given in the units of $\frac{\pi}{6c_o}$), c_o being the height of the unit cell of HCP titanium in the real space. We find that the acoustic phonons in these polymorphs are dominant at $\mathbf{q} \sim 0.6\frac{\pi}{6c_o}$, similar to that in martensitic phases of shape-memory alloys.
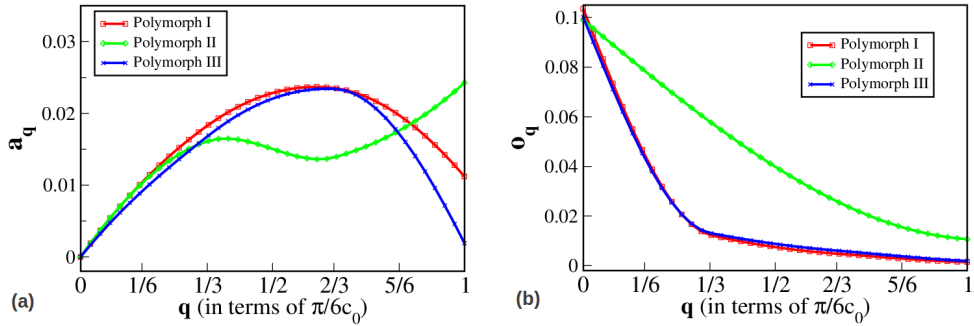

Figure 3.12: Inhomogeneous displacements in Ti polymorphs in Fourier space

The periodic displacement field of optical phonons $o_i^{(s)}$ (Equation 3.5), signifying internal strains built in the polymorph relative to the HCP structure, show an average value of around 0.1 for the three polymorphs (see Fig. 3.11b). Fourier analysis (Fig. 3.12b) reveals the dominance of optical modes at wavevector, $\mathbf{q} \to 0$, associated with the internal strains which show primarily long-wavelength variations.

3.4 Conclusions

Our theoretical results affirm the continuous nature of plastic flow at nanoscales in HCP metals, as reported for single-crystal Ti-5 at.% Al alloy [5]. This increased plasticity is attibuted to the occurrence of polymorphs of HCP metals with an exception of Zn, resulting from the interations of planar faults at nanoscale, and with ~ 0 energy cost of formation, relative to the respective hcp structures. The morphology of these long periodic polymorphs show a combination of homogeneous and inhomogeneous strain, and internal strain, having negligible correspondence with the local structure of stacking faults in crystals. This strongly indicates the 'deformation-induced polymorphism' is yet another mechanism contributing to plasticity in submicrometer-sized HCP metals, at low- and elevated temperatures.

Chapter 4

Temperature-dependent stability of stacking faults on (001) and (111) planes of Ni$_3$Al: First-principles analysis

4.1 Introduction

Nickel-base superalloys form a class of unique high-temperature materials, suitable for extensive applications in components of gas turbine blades and vanes in aircraft engines, and heat exchangers [32]. The strengthening of these superalloys is achieved from coherent precipitation of nano-scale γ'-phase of Ni$_3$Al (L1$_2$ structure) in γ-phase of Ni (FCC structure) [33, 34]. The ordered phase Ni$_3$Al, having superior creep-rupture properties, plays a significant role in conferring strength to the superalloy. Interestingly,the

yield stress of Ni_3Al increases with increasing temperature, which further augments its importance in high-temperature technological applications [32].

The dislocation structure of Ni_3Al is characterized by anti-phase boundaries (APB) [7, 35, 36] on {111} and {001} planes, $\frac{1}{3}\langle 121 \rangle$ superpartials bounding an intrinsic stacking fault (SISFs) [37, 38], and $\frac{1}{6}\langle 121 \rangle$ Shockley partials bounding a complex stacking fault (CSFs) [39] on the {111} planes. The anomalous yield stress has been studied with theoretical models based on experimental observations [40–46] and slip mechanisms based on atomistic simulations [6]. It is attributed to the interplay between thermal activation and cross-slip from the {111} octahedral plane to {001} cube plane. Additionally, the anisotropy of APB energies on the two planes, and high CSF energy have been suggested as the main driving force for this unusual high-temperature behavior. The nature of the underlying mechanism of slip at elevated temperatures is not clear and provides an impetus to first-principles study of high-temperature energetics of planar faults in Ni_3Al.

Atomistically, the energetics of slip at $0K$ can be estimated by employing the concept of generalized stacking fault (GSF) energy surface (or the γ-surface), as originally proposed by Vitek(1968). The γ-surface represents the energy cost of shearing one-half of the perfect crystal relative to the other as a function of generalized displacement $(\mathbf{f})$ in the plane. This has been analyzed by Rice suggesting that the energy released during dislocation nucleation is proportional to the unstable stacking fault energy (γ_{usf}) or the minimum energy barrier for slip along a particular direction [47]. The slip

process at finite temperatures can be analyzed by calculating energies of planar faults, taking into account the contributions of lattice vibrations to free energies [30]. This knowledge appears promising in resolving the cause of anomalous yield stress in Ni_3Al.

Our goal here is to study the energies of planar faults at $0K$ and at finite temperatures, and to associate the trends in the fault energetics with the unique flow behavior in Ni_3Al. To realize this goal, the remainder of the paper is organized as follows: Section 2 reviews the details of first-principles quantum mechanical methods employed in this study. In Section 3, we discuss the geometrical details of the unit cells employed for calculation of fault energies. The energetics of faults, and their corresponding influence on the electronic structure and phonon frequencies are discussed in Section 4. In Section 5, we estimate the change in fault energies as a function of temperature, taking into account the vibrational contributions to free energies. We conclude in Section 6, with a physical implication of the present theoretical study in the explanation of deformation process at finite temperatures.

4.2   Computational Details

Our calculations are based on first-principles density functional theory (DFT) and plane-wave pseudopotential method as implemented in Quantum ESPRESSO (QE) [20]. The ionic core-valence electron interactions are modelled using ultrasoft pseudopotentials [21] and electronic exchange-correlation energy is approximated with a local density approximation (LDA) as parameterized

by Perdew-Zunger [24]. Kohn-Sham wave functions are expanded in a plane-wave basis set truncated with energy cutoff of 30 Ry (and a corresponding cutoff of 240 Ry for charge density). Integrations over Brillouin zone are sampled with a uniform (8x8x8) k-grid for the bulk Ni_3Al, and the atomic structures are relaxed using Broyden, Fetcher, Goldfarb, Shanno (BFGS)-based algorithm until the Hellman-Feynman forces on each atom are lower than 0.001 Ry/bohr. Fault energetics on (111) and (001) planes of Ni_3Al is determined by structural relaxations of the faulted supercells, generated by expansion of unit cells along [111] and [001] directions, as explained in Section 3.

Dynamical matrices and phonon frequencies of faulted structures of Ni_3Al are obtained using the DFT linear response [28] method, (Quantum ESPRESSO implementation), on a uniform mesh of (2x2x1) **q**-points. Assuming a weak dependence of volume as a function of temperature, vibrational contributions to free energies are estimated within a harmonic approximation [29,30] given by

$$F_{vib} = E_{total} + \frac{k_B T}{N_q} \sum_{q,i} \log \left[2 \sinh \left(\frac{\hbar w_{iq}}{2 k_B T} \right) \right] \tag{4.1}$$

where N_q is the number of **q**-points on a finer mesh in the Brillouin zone, and ω_{iq} is the frequency at wave vector **q** obtained using Fourier interpolation of dynamical matrices at the (2x2x1) mesh of q-points obtained with DFT linear response.

4.3   Geometry and the γ-surface

The unit-cell geometries of L1$_2$ crystal structure of Ni$_3$Al along [001] and [111] directions, subsequently used for study of fault energetics on (001) and (111) planes, are shown in Fig. 4.1 and 4.2. Supercells with three unit cells along [111]-direction i.e. 36-atom system, and four unit cells along the [001]-direction i.e. 16-atom system are generated, and energies are calculated at fault vectors ($\mathbf{f}_i$) in the symmetry-irreducible wedges.
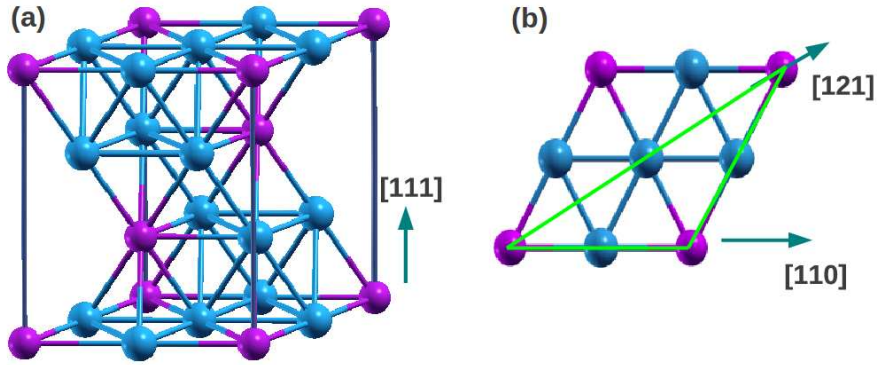

Figure 4.1: Unit cell of Ni$_3$Al for study of fault energetics on (111) plane, viewed (a) perpendicular to (111) plane, (b) along [111] direction. The triangle delineated in green (in (b)) shows symmetry-irreducible wedge used in calculation of fault energies.

The stacking fault energies (SFEs) are determined with:

$$\gamma_{SFE} = \frac{E_{faulted} - E_{pristine}}{Area} \tag{4.2}$$

The discrete SFEs are, then, Fourier interpolated over uniform (4x4) and (6x6) grids on (001) and (111) planes respectively, to obtain the generalized stacking fault (GSF) energy surfaces or the γ-surfaces.
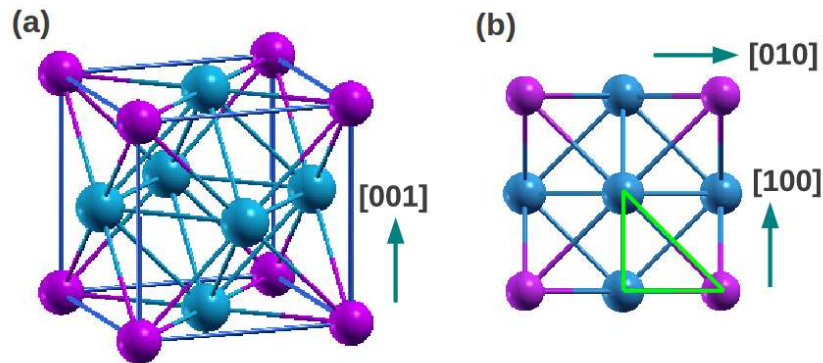
Figure 4.2: Unit cell of Ni$_3$Al for study of fault energetics on (001) plane, viewed (a) perpendicular to (001) plane, (b) along [001] direction. The triangle delineated in green (in (b)) shows symmetry-irreducible wedge used in calculation of fault energies.

4.4   Results and Analysis

Our theoretical prediction of lattice constant of bulk Ni$_3$Al (3.47$\mathring{A}$) is underestimated by 2.5% compared to the experimental results (3.56$\mathring{A}$) [48], which is within the typical DFT-LDA error. Inclusion of the spin polarization results in no change in the lattice constant of bulk Ni$_3$Al. The phonon frequencies over the entire k-point range are positive, confirming the local stability of the bulk Ni$_3$Al (Fig. 4.3). The phonon spectrum agrees well with the theoretical calculations by Isaev *et al.* and Wang *et al* [49,50], and is also in good agreement with experimental spectrum [51] along Γ-X and Γ-M directions, but shows discrepancy along Γ-R segment. As already pointed out by Isaev *et al.*, this is due to numerical instability, which may be resolved by increasing the convergence parameter in the calculation of force constants. However, this phonon spectrum is acceptable, as we focus on the changes in free energies associated with the phonon frequencies upon the introduction
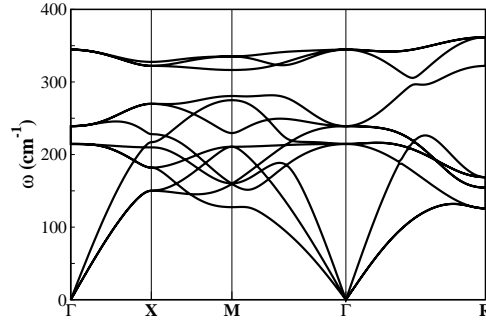
of planar faults.

Figure 4.3: Vibrational spectra of bulk Ni_3Al

4.4.1 Slip at $0K$

The γ-surface on the (111) plane of Ni_3Al (see Fig. 4.4) highlights the $[1\bar{1}0]$ direction as the energetically feasible slip direction with a minimum energy barrier of 0.37 J/m^2 at $\sim \frac{1}{4}[1\bar{1}0]$, on the path to an anti-phase boundary (APB) configuration at $\frac{1}{2}[1\bar{1}0]$ with a formation energy of 0.227 J/m^2. Our estimate of the $APB_{(111)}$ energy is higher than the experimental value of 0.180 J/m^2 [38,44] and that calculated by Mahesh et $al.$ [36], but is close to the earlier theoretical findings of Mryasov et $al.$ [6] and Rosengaard et $al.$ [7].

The atomic structure of $APB_{(111)}$ shows no change in the coordination number of atoms, and negligible difference in the electronic density of states at energies close to Fermi energy (E_F) with respect to the bulk Ni_3Al. The phonon density of states (Fig. 4.5a) highlight the local stability of the $APB_{(111)}$, and also reveals hardening of the high energy modes, pointing at the strengthening effects of $APB_{(111)}$ during the deformation process. Also, the density
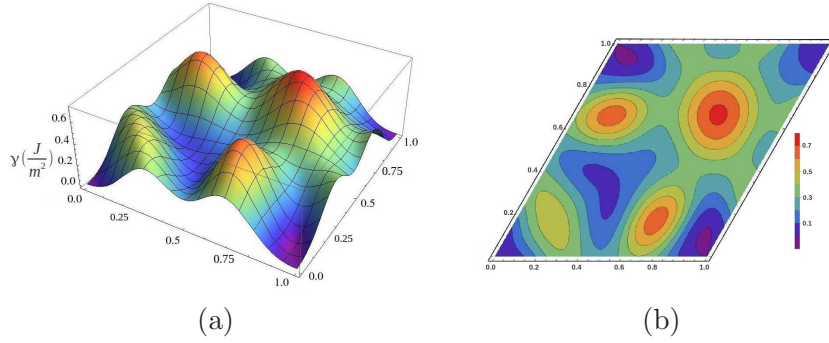
Figure 4.4: Fault energetics on (111) plane of Ni_3Al: (a) γ-surface, (b) contour plot

of modes in the frequency range, $100 < \omega > 150$, increases $APB_{(111)}$. The stiffening of high-energy modes and softening of low-energy modes can be qualitatively mapped to the compression and elongation of bonds in the relaxed structure with reference to the bond lengths in the pristine Ni_3Al, as is evident from the distribution of bond lengths ($D(\mathbf{b})$) in $APB_{(111)}$ (Fig. 4.5b).

The symmetry of $(111)[1\bar{1}0]$ GSF energy curve about the $\frac{1}{2}[1\bar{1}0]$ and the local stability of the $APB_{(111)}$ confirm the occurrence of dislocation dipoles on the (111) plane [40, 42], and the feasibility of dissociation reaction:

$$a_o[1\bar{1}0] \rightarrow \frac{a_o}{2}[1\bar{1}0] + APB + \frac{a_o}{2}[1\bar{1}0] \qquad (4.3)$$

at the onset of slip along $(111)[1\bar{1}0]$ slip system.

Further, low energy of the $ISF_{(111)[1\bar{2}1]}$ configuration (0.081 J/m^2) with respect to the $APB_{(111)[1\bar{1}0]}$ suggests an additional pathway for the initial slip along
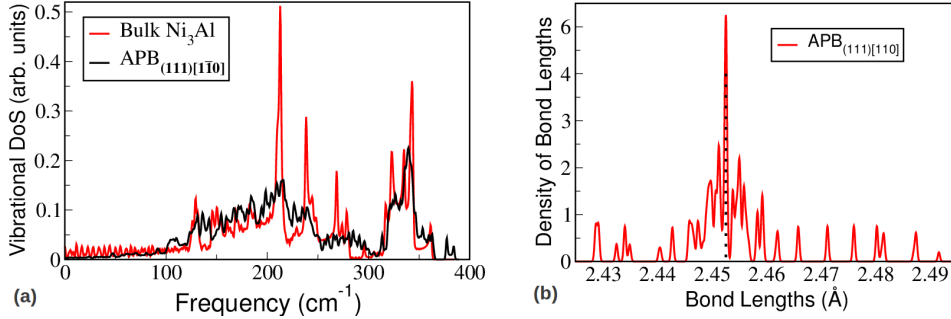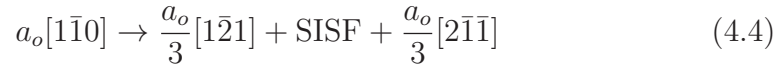
Figure 4.5: Structural features of APB$_{(111)[110]}$, (a) vibrational density of states, (b) density of bond lengths

[1$\bar{1}$0] direction, and an occurrence of dissociation reaction on {111} plane:

$$a_o[1\bar{1}0] \rightarrow \frac{a_o}{3}[1\bar{2}1] + \text{SISF} + \frac{a_o}{3}[2\bar{1}\bar{1}] \tag{4.4}$$

These dislocation partials occur on two {111} planes, aligned at 60° to each other, enclosing an intrinsic stacking fault. Our estimate of the ISF energy is higher than the experimental value of 0.015 J/m^2 [38, 43], but is close to the earlier theoretical results of Mryasov et $al.$ [6]. The ISF configuration derives its lower energy from its atomic structure, that maintains the nearest neighbors of each atom and shows negligible changes (within $\pm$ 0.02$\mathring{A}$) in the bond lengths on relaxation with respect to the bulk Ni$_3$Al. The local stability of this structure is confirmed from its vibrational spectrum (Fig. 4.6b), showing positive frequencies over the entire $\mathbf{q}$-point range. The electronic structure of the ISF configuration, with ABC∥BCABC type stacking, shows a slight increase in the electronic density of states at Fermi energy (Fig. 4.6a) relative to that of the pristine Ni$_3$Al.
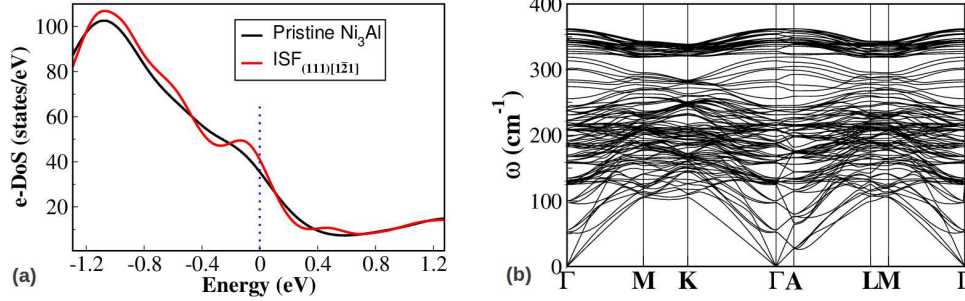
Figure 4.6: Electronic and atomic structural features of ISF$_{(111)[1\bar{2}1]}$, (a) vibrational spectrum, (b) electronic density of states

The proposed mechanism of formation of SISFs along $[1\bar{2}1]$ direction on the basis of energy difference between the APB$_{[1\bar{1}0]}$ and ISF$_{[1\bar{2}1]}$ configurations presents no insight into the nucleation of dislocation partial at $\sim \frac{1}{6}[1\bar{2}1]$ (i.e. unstable stacking fault configuration) with a high energy of about 0.464 J/m^2. Delving further, we find that the vibrational spectrum shows phonon instabilities at the Γ-point i.e. $\mathbf{q}=(0,0,0)$ (see Fig. 4.7a) of the USF configuration, with the eigendisplacements of atoms localized at the fault plane (see Fig. 4.7b). As suggested by Clutterbuck $et.$ $al.$ [52], the phonon instabilities significantly reduce the stress required for slip along a direction. This signifies that, in the case where phonon instabilities occur, the energy required for nucleating a dislocation partial is lower than the unstable stacking fault energy along that direction. The lowering of energy barrier because of the vibrational effects affirms the splitting of dislocation along $[1\bar{1}0]$ into two dislocation superpartials along $\langle 121 \rangle$ with the formation of 'superdislocation intrinsic stacking fault', SISF at $\frac{1}{3}[1\bar{2}1]$ in Ni$_3$Al [38].

Furthermore, taking into account the asymmetry of energetics along the $[1\bar{2}1]$
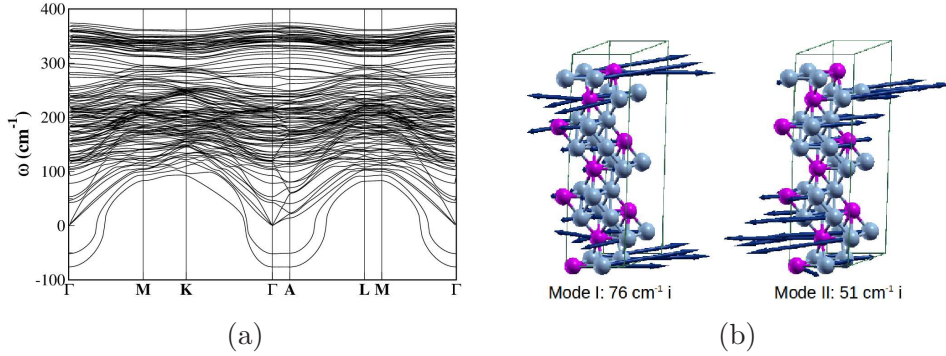
Figure 4.7: Phonon instability in USF configuration on (111) plane of Ni$_3$Al, (A) vibrational spectrum, (b) eigenvectors of unstable phonons

direction, there is a possibility of dissociation of $\frac{1}{2}[\bar{1}10]$ dislocation into two partials viz $\frac{1}{6}[\bar{1}2\bar{1}]$ and $\frac{1}{6}[\bar{2}11]$ with an approximate fault energy of 0.237 J/m^2, leading to lowering of the elastic strain energy. The resulting structure is locally stable, as is evident from the phonon density of states (Fig. 4.8), and shows a slight increase in the frequency of high energy modes from 362 cm^{-1} to 381 cm^{-1} with reference to the bulk Ni$_3$Al. This can be related to the change in bond lengths around the fault plane, similar to that in the APB$_{(111)}$ structure. This correspondence with the APB$_{(111)}$, along with the close energetics, owes to the similar changes in the local atomic structure causing Al atoms to become the nearest neighbors in both the structures. The local stability of this configuration with the fault vector $\frac{1}{6}[\bar{1}2\bar{1}]$ confirms the feasibility of formation of Shockley partials (or complex stacking fault, CSF) in Ni$_3$Al:

$$\frac{a_o}{2}[\bar{1}\bar{1}0] \rightarrow \frac{a_o}{6}[\bar{1}2\bar{1}] + \frac{a_o}{6}[21\bar{1}] \tag{4.5}$$

We now analyze the γ-surface on the (001) plane (Fig. 4.9) to determine the
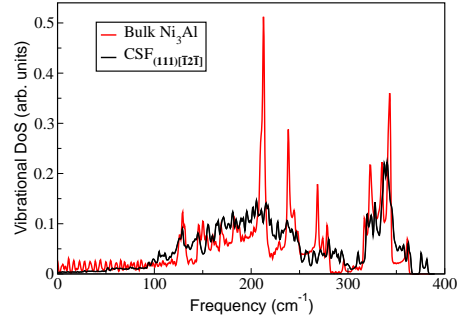
Figure 4.8: Vibrational density of states of $\frac{1}{6}[\bar{1}2\bar{1}]$ configuration on (111) plane of Ni$_3$Al

feasibility of slip along this plane. The extremal points on the (001) γ-surface highlight the USF energy i.e. minimum energy barrier of 1.35 J/m^2 along $\frac{1}{2}[1\bar{1}0]$ direction, with a relatively low ISF energy of $\sim$0.093 J/m^2 at $\frac{1}{2}[1\bar{1}0]$. The ISF energy agrees well with the experimental results of Sun *et al.* [53] and earlier theoretical estimates [36]. This ISF configuration corresponds to the APB on the (001) plane at $\frac{1}{2}[1\bar{1}0]$, which preserves the nearest-neighbor coordination of the pristine Ni$_3$Al.
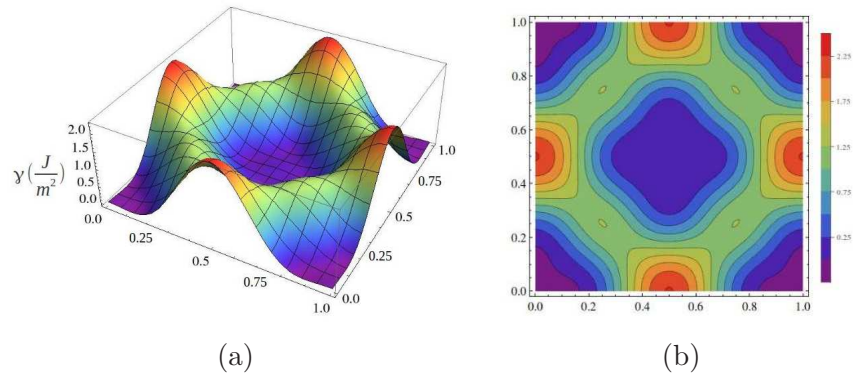

(a)   (b)

Figure 4.9: Fault energetics on (001) plane of Ni$_3$Al: (a) γ-surface, (b) contour plot

Analyzing the local atomic structure of the USF configuration, we find a decrease in the coordination number of atoms to 10, along with a significant

compression in bond lengths, essentially localized near the fault plane (Fig. 4.10a). These structural changes lead to phonon instabilities at the wavevectors (0,0,0) and $(0,0,\frac{1}{2})$ i.e. Γ- and Z-point in the Brillouin Zone respectively, as evident from its vibrational spectrum (Fig. 4.10b). Similar to the $USF_{(111)}$ structure exhibiting phonon instabilities, the calculated energy barrier height along $(001)[1\bar{1}0]$ slip system is not indicative of the energy required to nucleate a dislocation. Nevertheless, the energy barrier along $[1\bar{1}0]$ direction is significantly higher for a primary slip to occur on (001) plane at low stresses.

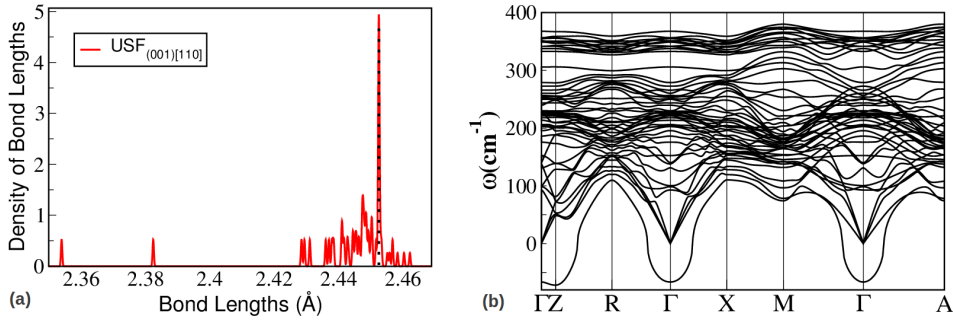Figure 4.10: Structural features of $APB_{(001)[110]}$, (a) density of bond lengths, (b) vibrational spectrum

Contrary to this high energy barrier, the low ISF energy of ~ 0.093 J/m^2 favors the occurrence of slip on the (001) plane. This is further supported by the local atomic structure showing no change in the nearest-neighbor, and minimal change in inter-atomic bond lengths. As a result, the local stability of this configuration is maintained (see Fig. 4.11b) over the entire Brillouin Zone. The slightly higher energy of this configuration with a distinct atomic structure, compared to the pristine Ni$_3$Al, correlates with increase in the electronic density of states close to Fermi level (see Fig. 4.11a). The energy

of APB configuration on (001) plane suggests the feasibility of occurrence of this structure during the slip process, but does not provide insight into the mechanism of transition of octahedral $\{111\}$ to cube $\{001\}$ slip in Ni_3Al. To understand this as possibly a temperature-dependent slip process, we study the fault energies as a function of temperature, by estimation of vibrational contributions to their free energies.
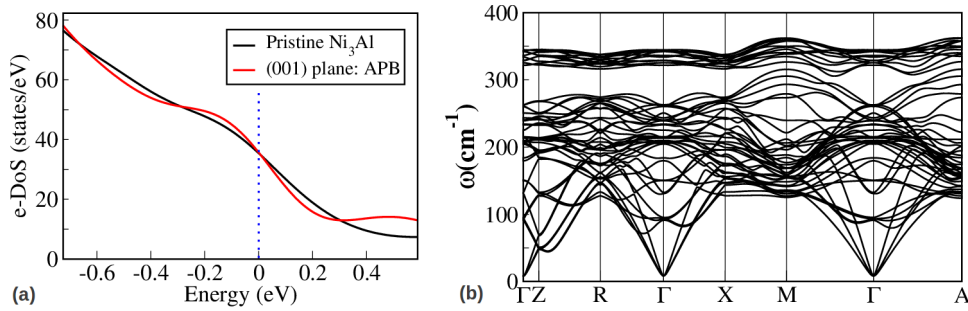

Figure 4.11: Electronic and atomic structural features of $ISF_{(001)[1\bar{1}0]}$, (a) electronic density of states, (b) vibrational spectrum

4.4.2 Analysis of planar faults at finite temperatures

Vibrational free energy of $APB_{(111)[1\bar{1}0]}$ is slightly positive (~ 4 mJ/m^2) relative to the pristine Ni_3Al structure, and increases with increase in temperature (see Fig. 4.12 and 4.13a). This indicates that the $APB_{(111)[1\bar{1}0]}$ formation is feasible at lower temperatures, owing to relatively lower energy barrier along the $[1\bar{1}0]$ direction, but as the temperature increases, the dissociation of $[1\bar{1}0]$ to form SISF and CSF will be more pronounced. The $ISF_{(111)[1\bar{2}1]}$ energy shows a monotonous decrease in vibrational free energy from $0K$ to 80% of the melting temperature of Ni_3Al (Fig. 4.13b), signifying widening of the stacking faults as a function of temperature, as observed by Lours *et*

al. [45]. The wide stacking faults decrease the tendency of a dislocation to cross-slip, thus inhibiting the movement of dislocation. This increases the flow stress on (111) plane of Ni_3Al.

Contrarily, the free energy of CSF decreases with temperature, suggesting an increased rate of dissociation of $\frac{1}{2}[1\bar{1}0]$ dislocation into Shockley partials along $[\bar{1}2\bar{1}]$ direction. The fault energy of these partials remains high ($\sim$220 mJ/m^2) at higher temperatures indicating narrow stacking faults. This increases the probability of cross-slip from $(111)[1\bar{1}0]$ slip system to $(001)[1\bar{1}0]$, with the formation of $APB_{(001)[1\bar{1}0]}$.

Further, the decrease in free energy of $APB_{(001)[1\bar{1}0]}$ (Fig. 4.12 and 4.13c) as a function of temperature supports the transition of slip process from octahedral ({111}) plane to cube ({001}) plane. The increase in dislocation density along the (111) plane and (001) plane in tandem, further leads to locking of dislocation, thus influencing the overall flow stress behavior of Ni_3Al.

4.5   Conclusions

The fault energies on (111) and (001) planes of Ni_3Al show a feasibility of initial slip along $(111)[1\bar{1}0]$ slip system. Two types of dissociation reactions are possible energetically, (1) formation of superdislocation intrinsic stacking faults, and (2) formation of Shockley partials. These dislocation partials determine the flow stress behavior of Ni_3Al at elevated temperatures. The
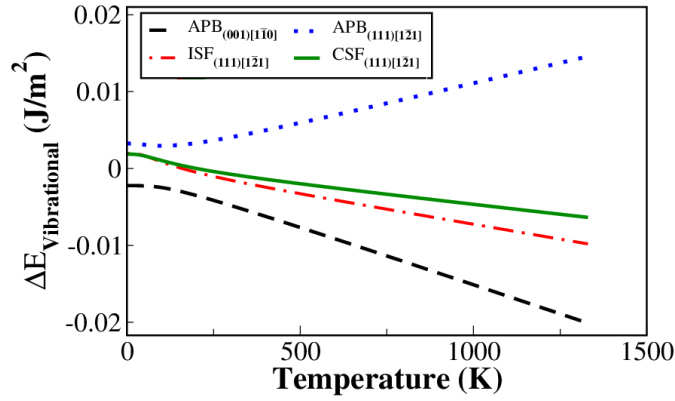
Figure 4.12: Temperature-dependent vibrational free energies of faults relative to pristine Ni$_3$Al
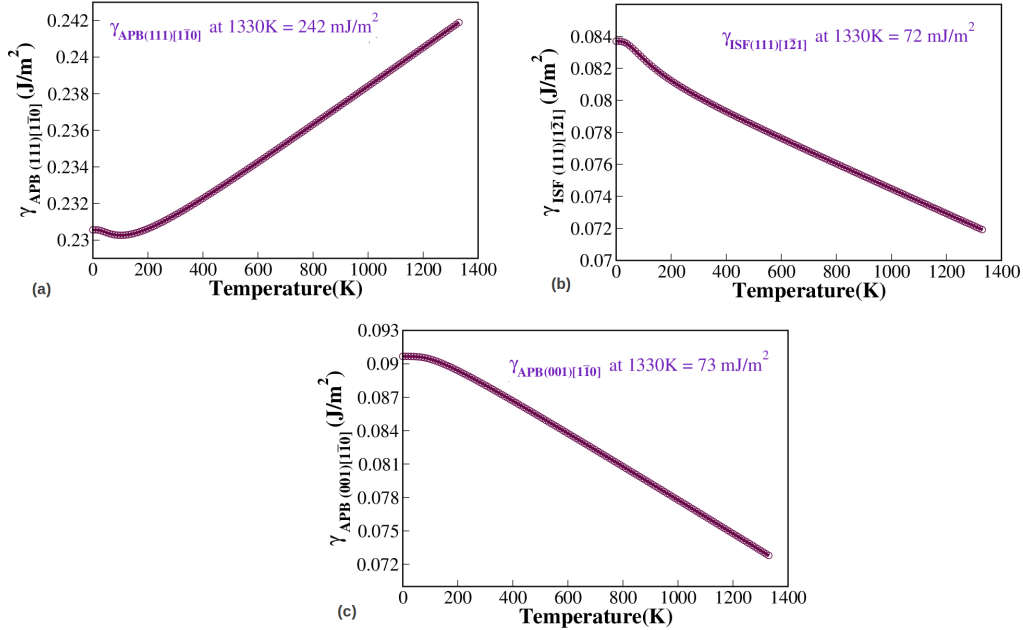
Figure 4.13: Fault energies of, (a) APB$_{(111)[1\bar{1}0]}$ (increase by 5 %), (b) ISF$_{(111)[1\bar{2}1]}$ (decrease by 14 %), and (c) APB$_{(001)[1\bar{1}0]}$ (decrease by 20 %), when the temperature increases from 0 to 1330 K

increase in yield strength in Ni$_3$Al as a function of temperature is because of the activation of slip on both {111} and {001} planes, due to widening

of stacking faults and tendency of a dislocation to cross-slip, leading to decreased mobility of dislocations.

Chapter 5

Temperature-dependent stability of stacking faults in FCC metals: First-principles analysis

5.1 Introduction

The mechanism of plastic deformation in a material is governed by energetics of nucleation and movement of a dislocation, and the nature of its interactions with other dislocations [2]. Along a particular slip system of a crystal, the energy of the strain field associated with a dislocation is proportional to the square of its Burgers vector [54]. As a result, the plausibility of activation of $\{111\}\langle110\rangle$ slip system in FCC metals should be apparently higher than that along the $\{111\}\langle121\rangle$ slip system. Secondly, the tendency of a dislocation to

dissociate into two or more dislocations can assist in reduction of the total strain energy of the system. Heidenreich and Shockley [55] suggested an example of one such dislocation reaction on the {111} plane of FCC metals:

$$\frac{a_o}{2}[10\bar{1}] \rightarrow \frac{a_o}{6}[2\bar{1}\bar{1}] + \frac{a_o}{6}[11\bar{2}], \text{in terms of Burgers vectors} \qquad (5.1)$$

The resulting dislocation partials enclose a stable stacking fault, with a condition that the decrease in energy due to dissociation must be greater than the increase in interfacial energy of the faulted region [54]. The stacking fault energy of a material influences the dislocation structure, thus affecting the defect density, strain-hardening rate, and high-temperature creep strength. Lower stacking fault energy leads to wider stacking faults which hinder the dislocation mobility, leading to an increased density of twins which act as dislocation sources [56, 57]. The lesser tendency of the dislocations to cross slip due to wider stacking faults reduces the rate of dynamic recovery, hence enhancing the creep strength of the material [58, 59].

The concept of generalized stacking fault (GSF) energy surface (or the γ-surface), which represents the energy cost of shearing one-half of the perfect crystal relative to the other as a function of displacement (**f**) in the plane, originally proposed by Vitek(1968), has been extensively used to study the energetics of dislocation nucleation and slip in crystals. The GSF energy surface has been analyzed further by Rice, showing that the energy release rate of dislocation nucleation is proportional to the unstable stacking fault energy (γ_{usf}) or the minimum energy barrier during slip along a particular

direction [47]. The GSF energy curves, obtained as sections of the γ-surface represent directional anisotropy of slip on a plane, and indicate the energy barrier configurations (saddle points), and an intrinsic stacking fault configuration (a local minimum). Prompted by the experimental evidence [60, 61] for the presence of stacking faults along $\{111\}\langle 121\rangle$ slip system in FCC metals, extensive theoretical studies [62–66] have been carried out using different interatomic potentials to understand the mechanism of slip along $[1\bar{2}1]$ direction. Nevertheless, it is pertinent to understand the energetics of slip over the entire $\{111\}$ plane of FCC metals, and gain insight into the local atomic structural changes upon the introduction of the planar faults.

Also, the temperature-dependent stacking fault energies are crucial in the understanding of slip process during warm working of a material, i.e. upto 70 - 80 % of the melting temperature, and also determining the creep behavior. The vibrational contributions to free energies at finite temperatures have been shown to effectively capture the phase diagram [67], changes in the stacking faults [68–70], and energetics of points defects. Though Hickel *et al.* have studied temperature-dependent intrinsic stacking fault energies in Ni, most of the earlier first-principles study of faults are at $0K$. In the present work, we calculate vibrational free energies of faults on (111) plane of FCC metals to estimate their temperature-dependent barrier heights and stacking fault energies.

The aim of our work is two-fold, (1) to understand the slip process in terms of the local stability and energetics of faults along $[1\bar{1}0]$ and $[1\bar{2}1]$ directions

on the (111) plane of FCC metals, and (2) to obtain temperature-dependent fault energies by calculating the vibrational contributions to free energies. Considering technological importance and applicability, we focus here on three FCC metals, viz aluminum, copper and nickel.

We describe the first-principles computational methods in Section II. The energetics of faults, and their reflections in the electronic structure and phonon frequencies are discussed in Section 3. In Section 4, we estimate the change in fault energies as a function of temperature, taking into account the vibrational contributions to free energies. We conclude in Section 5, discussing physical implications of the present analysis and a possible explanation of deformation process at finite temperatures.

5.2 Computational Details

Our calculations are based on first-principles density functional theory (DFT) and plane-wave pseudopotential method as implemented in Quantum ESPRESSO [20] (QE). The ionic core-valence electron interactions are modelled using ultra-soft pseudopotentials [21] and electronic exchange-correlation energy is approximated with a generalized gradient approximation (GGA) as parametrized by Perdew-Burke-Ernzerhof [23] for aluminum, Perdew-Wang [22] for copper, and with a local density approximation (LDA) as parameterized by Perdew-Zunger [24] for nickel. Kohn-Sham wave functions are expanded in a plane-wave basis set truncated with energy cutoff of 30 Ry (and charge density with a corresponding cutoff of 240 Ry). Integrations over Brillouin

zone are sampled with a uniform (15x15x8) k-grid for a 3-atom unit cell with its c-vector oriented along [111] direction of FCC metals, and atomic structures are relaxed using Broyden, Fetcher, Goldfarb, Shanno (BFGS)-based algorithm until the Hellman-Feynman forces on each atom are lower than 0.001 Ry/bohr. Supercells were constructed by tripling this cell to simulate planar faults. By tilting the c-vector of the supercell, a fault or localized shear deformation is introduced along [1$\bar{1}$0] and [1$\bar{2}$1] directions on the (111) plane. Atomic relaxations in these faulted supercells are carried out to attain minimum energy structures, and generalized stacking fault energies are calculated using:

$$E_{GSF} = \frac{E_{faulted} - E_{pristine}}{Area} \tag{5.2}$$

Dynamical matrices and phonon frequencies in the faulted structures of Al, Cu, and Ni are obtained using the DFT linear response [28] method on a uniform mesh of (3x3x1) $\mathbf{q}$-points. Assuming a weak dependence of volume as a function of temperature, and hence $\omega(T)$, vibrational contributions to the free energies are estimated within a harmonic approximation [67,68] given by

$$F_{vib} = E_{total} + \frac{k_B T}{N_q} \sum_{q,i} \log \left[2 \sinh \left(\frac{\hbar w_{iq}}{2 k_B T} \right) \right] \tag{5.3}$$

where N_q is the number of $\mathbf{q}$-points on (20x20x7) mesh in the Brillouin zone, and ω_{iq} is the frequency at wave vector $\mathbf{q}$ obtained using Fourier interpolation of dynamical matrices determined on the (3x3x1) mesh of q-points using DFT linear response.

5.3 Results and Analysis

Our theoretical estimates of lattice constants of Al, Cu and Ni are 4.05 $\mathring{A}$, 3.63 $\mathring{A}$, and 3.43 $\mathring{A}$, within typical DFT errors of the corresponding experimental values at room-temperature [71]. Phonon dispersion of the 3-atom unit cells of bulk Al, Cu, and Ni along the [111] direction (see Fig. 5.1) show real frequencies over the entire Brillouin Zone, confirming their local stability (see Fig. 5.2). The Γ-A$(0,0,\frac{1}{2})$ segment representing the height of the cell along [111]- direction in the reciprocal space reduces to one-third in the supercell, owing to Brillouin zone folding. The changes in this segment on the introduction of planar faults are the fingerprints of structural changes occurring in the faulted configurations of Al, Cu, and Ni.
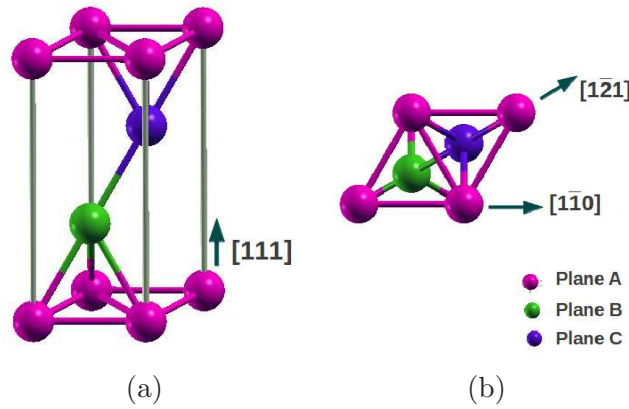

(a)   (b)

Figure 5.1: FCC unit-cell with ABCABC stacking along [111] direction, (a) front view, and (b) view along [111] direction. The shortest Burgers vector is $\frac{a_o}{2}[1\bar{1}0]$, a_o: lattice constant of conventional unit cell
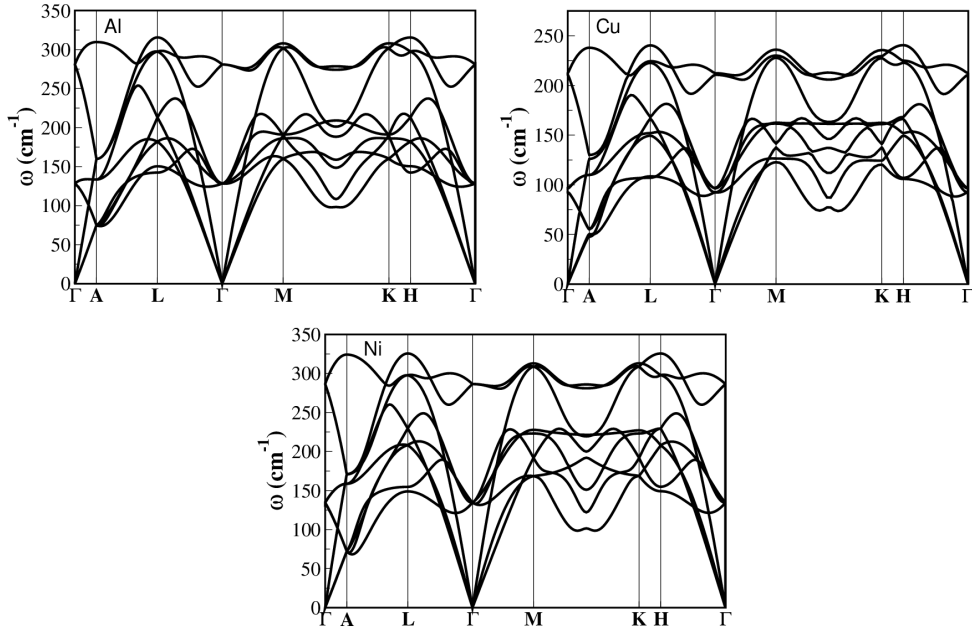
Figure 5.2: Phonon Spectra of bulk Al, Cu and Ni

5.3.1 Analysis of planar faults at 0 K

The generalized stacking fault energy curves on the (111) plane of Al, Cu and Ni (see Fig. 5.3) show directional anisotropy, with no local minimum along $[1\bar{1}0]$, and a local minimum i.e. intrinsic stacking fault configuration and a minimum energy barrier i.e. unstable stacking fault configuration along $[1\bar{2}1]$ direction. The minimum energy barriers, and ISF energy on the (111) plane of Al, Cu and Ni are tabulated in Table 1.

The comparable energy costs of nucleation of dislocation along $[1\bar{1}0]$ and $[1\bar{2}1]$ directions in Al suggests the feasibility of slip along $[1\bar{1}0]$ direction, contrasting to the nature of fault energetics in Ni. The slip in Al along $[1\bar{2}1]$ direction results in an intrinsic stacking fault of energy comparable to the barrier height with $\frac{\gamma_{isf}}{\gamma_{usf}}$ ratio close to unity. This implies a higher
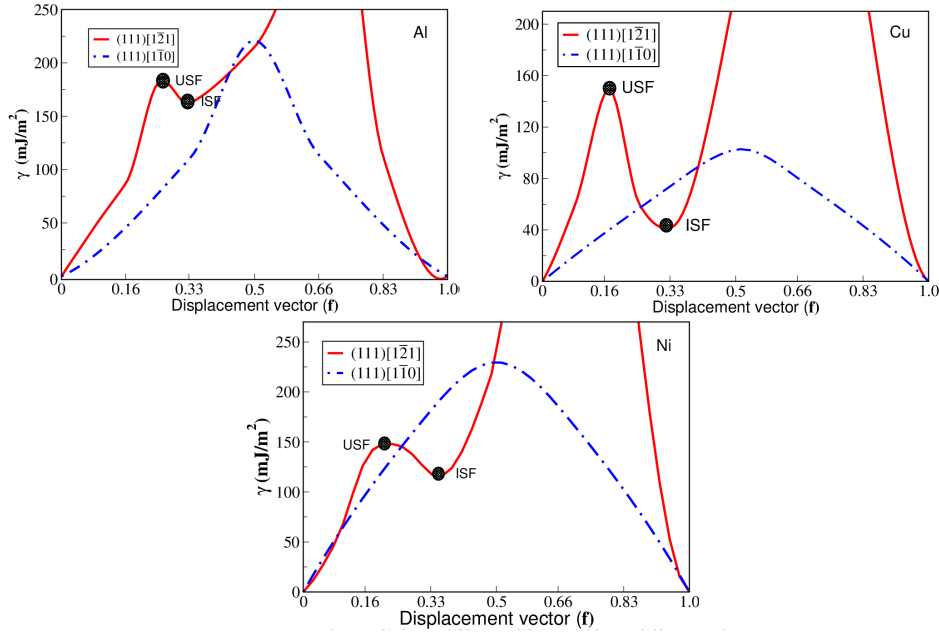
Figure 5.3: Generalized stacking fault energy curves for $[1\bar{1}0]$ and $[1\bar{2}1]$ directions on (111) plane of Al, Cu and Ni

tendency of propagation as a full dislocation along $[1\bar{2}1]$ direction than as dislocation partials with an enclosed stacking fault, supporting the suggestion of Swygenhoven *et.al.* in terms of the energy cost of a trailing partial after an initial dislocation partial has been nucleated [63]. In Cu, the energy barriers of slip along $[1\bar{1}0]$ and $[1\bar{2}1]$ directions suggest that the $(111)[1\bar{1}0]$ slip system is more favorable, but a very low intrinsic stacking fault energy suggests the

Table 5.1: Stacking fault energies in Al, Cu and Ni

	γ_{isf} (mJ/m^2)	γ_{usf} (mJ/m^2)	$\frac{\gamma_{isf}}{\gamma_{usf}}$
Al	**162**, 166[†], 165[#], 146[§]	**181**, 151[§]	**0.90**
Cu	**42**, 45[†], 33[§]	**149**, 173[§]	**0.27**
Ni	**117**, 125[†], 120[§], 121[Φ]	**148**, 172[§], 230[Φ]	**0.79**

Values in bold: Present work

[†]$\gamma_{experimental}$ [72], [#]Lu *et al.* [2], [%]Swygenhoven *et al.* [63], [Φ]Aditi *et al.* [73]

dissociation of $\frac{1}{2}[1\bar{1}0]$ dislocation into $\frac{1}{6}[1\bar{2}1]$ partials with a stacking fault, overcoming the high energy barrier of unstable stacking fault at $\sim \frac{1}{12}[1\bar{2}1]$.

Our estimate of $\frac{\gamma_{isf}}{\gamma_{usf}}$ value of 0.79 for Ni corresponds with that obtained using MishinFarkas Ni potential (0.69) [63], does not agree with the earlier reported DFT value of 0.53 [73]. This inconsistency in $\frac{\gamma_{isf}}{\gamma_{usf}}$ value with earlier results makes it infeasible to interpret the fault energies in Ni in terms of propagation as a full dislocation along $[1\bar{2}1]$, as in Al, or as dislocation partials, like in Cu. Elastic strains i.e. the ratio of the fault vector at the onset of dislocation nucleation to the length of Burgers vector along $[1\bar{2}1]$ direction in Al, Cu, and Ni are $\sim$0.25, $\sim$0.16, and $\sim$0.25, agreeing well with the results of Ogata *et al.* [74] for Al and Cu.

Electronic density of states (e-DoS) in Al, Cu, and Ni show interesting features near the Fermi level. In Al, there is an increase in the density of states close to Fermi level in the USF and ISF configurations along $[1\bar{2}1]$ direction (see Fig. 5.4), suggesting an increased conductivity upon the introduction of faults. This is in contrast with Cu, where the density of states near the Fermi Level in the ISF configuration significantly change relative to that in pristine Cu. The e-DoS of faulted Ni is nearly the same as that of pristine Ni.

Next, we discuss the deformation mechanism on the {111} planes of Al, Cu, and Ni at 0 K by understanding the local atomic structures, and analyze the electronic and vibrational signatures of the faulted configurations at the
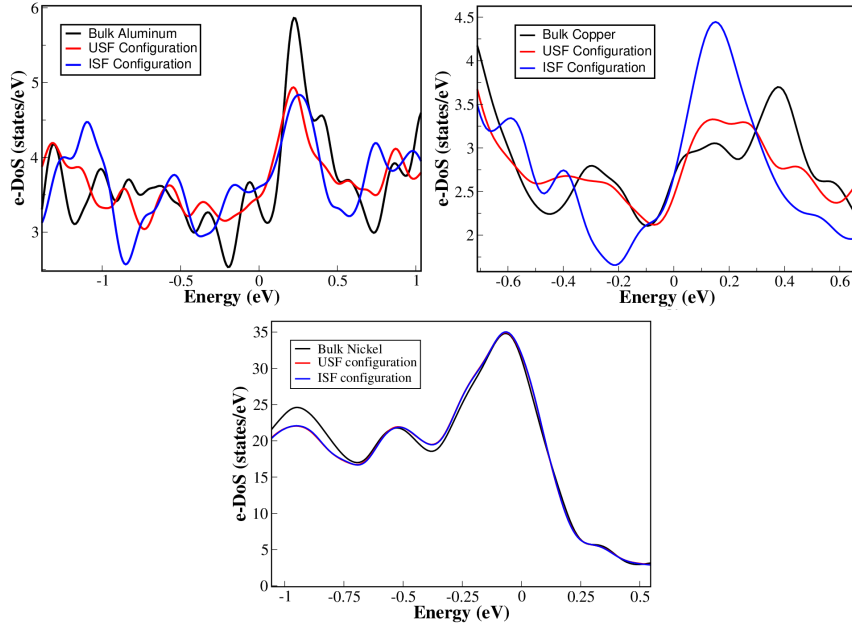
Figure 5.4: Electronic density of states in pristine and faulted structures of Al, Cu and Ni

extremal points of the GSF curves (Fig. 5.3).

5.3.2   Al

In Al, the energetic feasibility of slip along $[1\bar{1}0]$ and $[1\bar{2}1]$ directions is further confirmed by the local stability of minimum energy barrier configurations along both these directions, with the fault vectors $\frac{1}{4}[1\bar{1}0]$ and $\sim \frac{1}{8}[1\bar{2}1]$ respectively. This is evident in density of phonon states with only real frequencies in the two configurations (Fig. 5.5a). The softening of phonon modes (i.e. an increased density of modes with frequencies below 125 cm^{-1}) upon the introduction of planar faults, in reference to the bulk Al, suggests their dominance in the vibrational free energies of the system at higher temperatures. Furthermore, analysis of the distributions of bond lengths, D($\mathbf{b}$) for the two
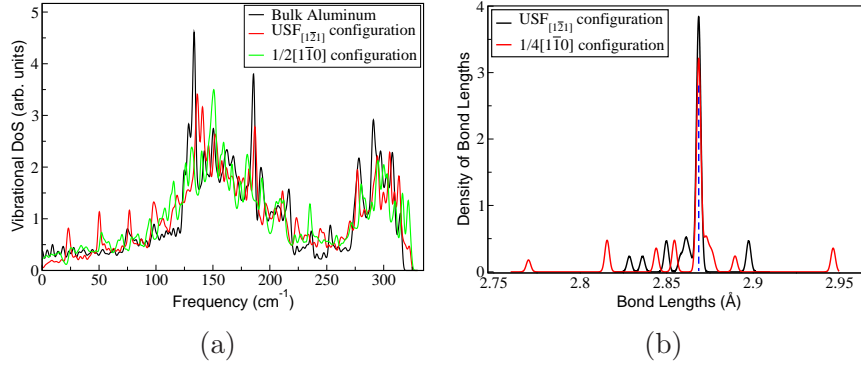
Figure 5.5: Comparison of energy barrier configurations along $[1\bar{1}0]$ and $[1\bar{2}1]$ directions on (111) plane of Al: (a) phonon density of states, (b) distribution of bond lengths, D(**b**). The dashed line, in (b), shows bond length of pristine Al.

configurations (Fig. 5.5b) reveal greater contraction and expansion of bonds resulting from slip along $[1\bar{1}0]$ direction, along with a decrease in coordination number of atoms on the fault plane to 11. The local stability of this configuration supports the experimental observation by Wert. *et al.* showing tendency of single slip in Al along $(111)[10\bar{1}]$ system [75].

Analysis of the minimum energy configuration i.e. ISF along $[1\bar{2}1]$ direction shows negligible change in the bond lengths i.e ± 0.006 $\mathring{A}$, with reference to that in pristine Al. The vibrational spectrum (Fig. 5.6) of this structure reveals the preservation of the local stability, and shows an increase in the frequency of high-energy optical modes at the Γ-point to $\sim$310 cm^{-1} from 281 cm^{-1} in the pristine Al.
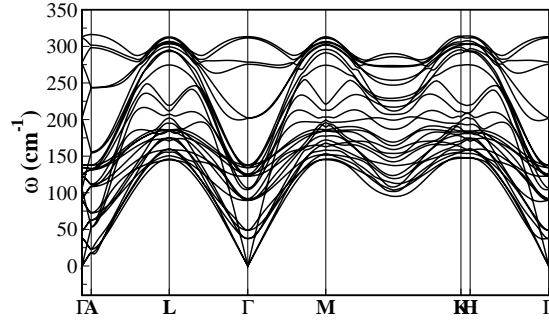
Figure 5.6: Vibrational spectrum of ISF configuration of Al

5.3.3   Cu

The lower energy of the slip along $[1\bar{1}0]$ direction as compared to the energy barrier along $[1\bar{2}1]$ on the (111) plane of Cu prompts the need to analyse the local structure of the configuration at $\frac{1}{4}[1\bar{1}0]$ and find an origin of the occurrence of the dissociation partials at $\frac{1}{6}[1\bar{2}1]$. The phonon DoS of the configuration with $\mathbf{f} = \frac{1}{4}[1\bar{1}0]$ shows local stability at the Γ-point (Fig. 5.7a), and hardening of high-energy optical modes, relative to that at the Γ-point of pristine Cu. The local stability seems to arise from the rearrangement of atoms away from the fault plane, leading to only weak contraction and expansion of the bonds (Fig. 5.7b), preserving the coordination number of atoms in the structure.

This suggests that the occurrence of stacking faults along $[1\bar{2}1]$ direction in Cu, resulting from the dissociation of perfect dislocation along $\frac{1}{2}[1\bar{1}0]$ into Shockley partials [54], is owing to a very low energy of the ISF configuration, in addition to the decrease in elastic strain energy. The ISF configuration is locally stable as reflected by $\omega \, ge \, 0$ over the Brillouin Zone (Fig. 5.8), with
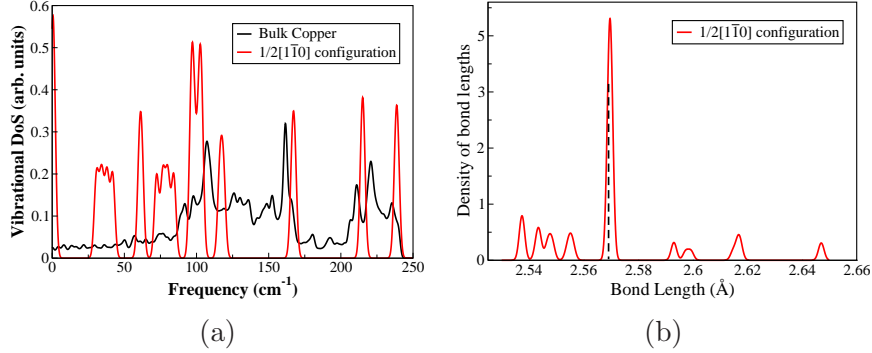
Figure 5.7: Energy barrier configuration along $[1\bar{1}0]$ direction on (111) plane of Cu: (a) phonon density of states (red curve shows v-DoS at Γ-point), (b) distribution of bond lengths, D(**b**). The dashed line, in (b), shows bond length of pristine Cu

change in the bond lengths within ± 0.004 $\overset{\circ}{A}$ as compared to that in pristine Cu. A very low energy of the ISF structure supports the formation of wide stacking faults in Cu, consistent with the experiments [60].
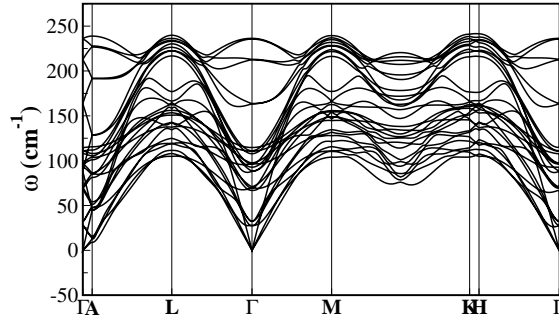

Figure 5.8: Vibrational spectrum of ISF configuration in Cu

The origin of formation of dislocation partials along $(111)[1\bar{2}1]$ system in Cu still remains unresolved, given the high unstable stacking fault energy along the $[1\bar{2}1]$ direction. Vibrational spectrum of the USF configuration (Fig. 5.9a) shows structural instabilities at Γ-point and at wavevector (0, 0,
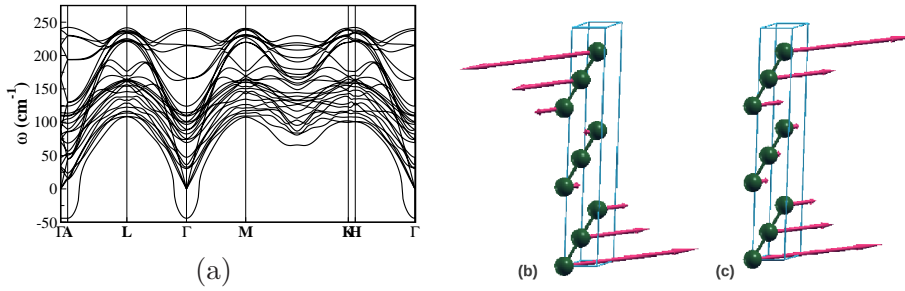
Figure 5.9: Local instability in Cu, (a) Vibrational spectrum of USF configuration, (b) and (c) eigenvectors of unstable modes at Γ- and A- point

$\frac{1}{2}$) i.e A-point, with an imaginary frequency of ~ 47 cm^{-1}i. The occurrence of local instability in the USF structure signifies that the energy barrier is overestimated, and thus is not indicative of the energy release rate during the dislocation nucleation along [1$\bar{2}$1] direction. This suggests the feasibility of nucleation of dislocation partials along [1$\bar{2}$1] direction, and formation of the stacking faults on the (111) plane of Cu. Further, the unstable modes involve eigendisplacements parallel to the fault plane (Fig. 5.9b and c), indicating the tendency of this configuration to attain a local minimum through shear distortion. The basis for this lattice instability lies in the local decrease in the coordination of atoms close to the fault plane to 11, with minimal change in the atomic planes away from the fault.

5.3.4 Ni

The mechanism of slip on the (111) plane of Ni is relatively straightforward owing to significant difference between the energy barriers along [1$\bar{1}$0] and [1$\bar{2}$1] directions. The local stability of the USF and ISF configuration, as is evident from their vibrational spectra (see Fig. 5.10a and 5.10b), further favors the feasibility of formation of dislocation partials along [1$\bar{2}$1] in Ni.

The local coordination number of atoms is maintained with no significant change (within ± 0.034 AA) in bond lengths in the USF structure.
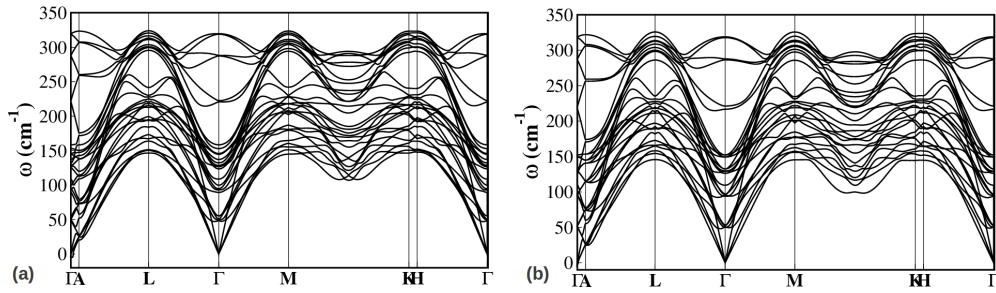

Figure 5.10: Vibrational spectra of (a) USF, and (b) ISF configurations of Ni

5.3.5 Analysis of planar faults at finite temperatures

We compare the temperature-dependent stability of three FCC metals, viz Al, Cu, and Ni, by estimating the vibrational contributions to free energies (F_{vib}) of their ideal structures from 0 K to about 80% of their melting temperatures (see Fig. 5.11). Our results correspond well with the earlier calculations by Alfè [76] on temperature-dependent vibrational free energies in bulk Al with phonon frequencies obtained using small displacement method. The free energy curves confirm the room temperature ($\sim$300 K) and high-temperature structural stability of bulk Al, Cu and Ni.

The change in the vibrational free energies of the faulted structures as a function of temperature is indicative of their stability and relative feasibilty of their occurrence during the process of deformation at elevated temperatures. The energy barriers in Al decrease from 214 mJ/m^2 to 167 mJ/m^2 along
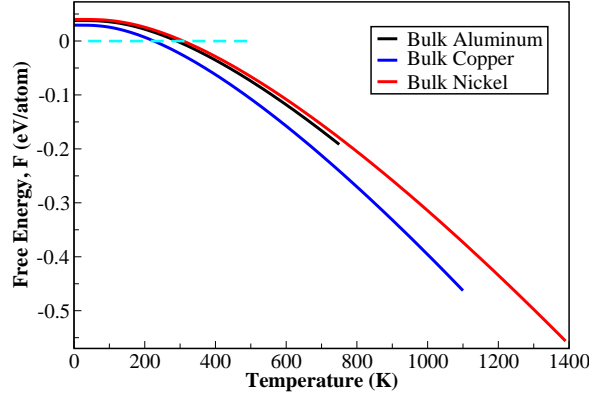
Figure 5.11: Temperature-dependent vibrational free energies of bulk Al, Cu and Ni

[1$\bar{1}$0], and from 175 mJ/m^2 to 134 mJ/m^2 along [1$\bar{2}$1], indicating a decrease by about $\sim$23 % when the temperature increases from 0 to 750 K (Fig. 5.12a). This is comparable to the decrease in the USF energy (γ_{usf}) for Ni, for temperature ranging from 0 K to 80 % of its melting point (Fig. 5.12b). The ISF energies (γ_{isf}) of Al, Ni and Cu show a decrease by 30%, 57% and 71% due to vibrational effects (see Fig. 5.13), signifying an increased tendency of formation of dislocation partials, leading to widening of stacking faults in these metals, when the temperature is increased from 0 K to 80 % of their melting temperatures.

5.4   Conclusion

The intrinsic stacking faults along [1$\bar{2}$1] direction on the (111) plane is seen to be generic to the FCC metals but their occurrence stems from different slip pathways, depending on local stability of the intermediate fault configurations. The vibrational spectra show increase in the density of soft phonon
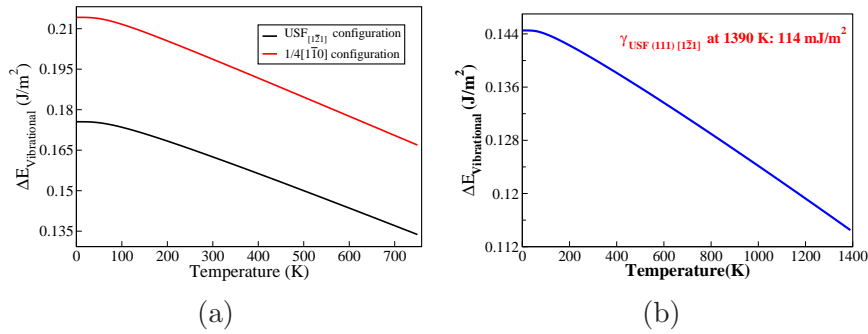
Figure 5.12: Comparison of the temperature-dependent energy barriers in (a) Al, and (b) Ni. The barrier height decreases by ∼23 % in Al along both the directions (from 0 to 760 K), and ∼20 % in Ni along [$1\bar{2}1$] (from 0 to 1390 K)
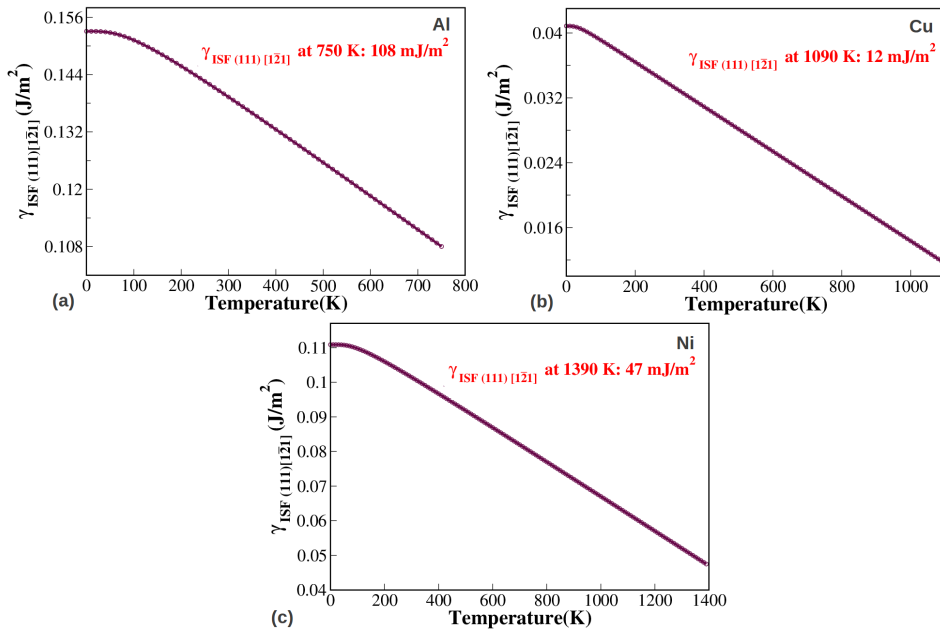

Figure 5.13: Temperature-dependent intrinsic stacking fault energies of (a) Al, (b) Cu, and (c) Ni. ISF energies decrease by 30%, 71% and 57% in Al, Cu, and Ni. Temperature range: 0 K − 80% T_M

modes (with frequencies ∼100 cm^{-1})in the faulted structures of each of these metals, signifying their dominant contributions to vibrational free energies at high temperatures. The vibrational contributions to free energies result

in decrease in the stacking fault energies by 30%, 71% and 57% in Al, Cu, and Ni, respectively, when the temperature is increased from 0 K to 80 % of their respective melting points.

Chapter 6

Summary and Conclusions

The interplay of physical entities namely stress, strain and temperature is shown in Fig. 6.1. This thesis details the first-principles study of stress-response in the form of strain ϵ, planar faults and nanoscale polymorphs in three classes of materials namely HCP metals, Ni_3Al and FCC metals.
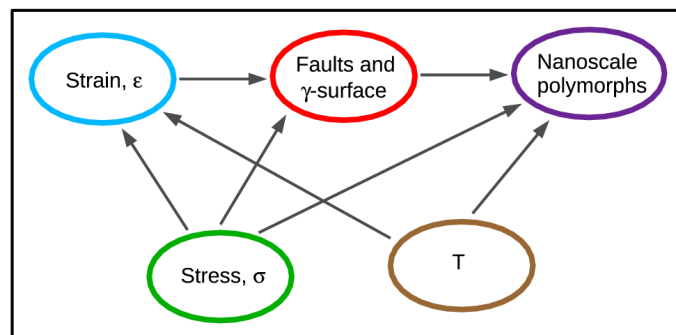

Figure 6.1: Interplay between stress, strain and temperature in materials

- The study of long-period nanoscale polymorphs in HCP metals, as presented in Chaper 3, can find its far-reaching relevance to experiments

in understanding the deformation mechanisms in small-dimension samples.

- The single-crystal nano-precipitates of γ' in γ-phase, known to confer high-termperature strength to nickel based-superalloys, form an important ingredient for turbine blades. The understanding of temperature-dependent deformation mechanism in γ'-phase Ni_3Al through the study of anisotropy of planar faults in Ni_3Al, as discussed in Chapter 4, explains the possible mechanism resulting in anomalous yield stress behavior of Ni_3Al.

- Analysis of temperature-dependent dislocation motion has been the motivation for study of planar faults in Al, Cu and Ni. The study, presented in Chapter 5, has led to two key points, (1) the energy of unstable displacement on the γ-surface need to be considered with caution, and (2) the stacking fault energies of Al, Cu and Ni significantly decrease with temperature, indicating a decrease in flow stress in these metals.

Bibliography

[1] J. W. Christian and V. Vitek, Reports on Progress in Physics **33**, 307 (1970).

[2] G. Lu, N. Kioussis, V. V. Bulatov, and E. Kaxiras, Phys. Rev. B **62**, 3099 (2000).

[3] M. Peters, J. Hemptenmacher, J. Kumpfert, and C. Leyens, in *Titanium and Titanium Alloys* (Wiley-VCH Verlag GmbH & Co., KGaA, 2005), pp. 1–36.

[4] Q. Yu *et al.*, Nature **463**, 335 (2010).

[5] Q. Yu *et al.*, Applied Physics Letters **100**, 063109 (2012).

[6] O. Mryasov, Y. Gornostyrev, M. van Schilfgaarde, and A. J. Freeman, Acta Materialia **50**, 4545 (2002).

[7] N. M. Rosengaard and H. L. Skriver, Phys. Rev. B **50**, 4848 (1994).

[8] R. Voskoboinikov, The Physics of Metals and Metallography **114**, 545 (2013).

[9] Y. feng WEN, J. SUN, and J. HUANG, Transactions of Nonferrous Metals Society of China **22**, 661 (2012).

[10] R. M. Martin, *Electronic Structure* (Cambridge University Press, UK, 2004).

[11] C. M. Byer, B. Li, B. Cao, and K. Ramesh, Scripta Materialia **62**, 536 (2010).

[12] C. Peng *et al.*, Applied Physics Letters **102**, 083102 (2013).

[13] J.-Y. Kim and J. R. Greer, Applied Physics Letters **93**, 101916 (2008).

[14] M. Lowry *et al.*, Acta Materialia **58**, 5160 (2010).

[15] Q. Yu, R. Mishra, and A. Minor, JOM **64**, 1235 (2012).

[16] I. Shin and E. A. Carter, Modelling and Simulation in Materials Science and Engineering **20**, 015006 (2012).

[17] S. Ogata, Y. Umeno, and M. Kohyama, Modelling and Simulation in Materials Science and Engineering **17**, 013001 (2009).

[18] R. M. Martin, *Electronic Structure* (Cambridge University Press, UK, 2004), pp. 512–518.

[19] J. Ye, R. K. Mishra, A. K. Sachdev, and A. M. Minor, Scripta Materialia **64**, 292 (2011).

[20] P. Giannozzi, J. Phys.: Condens. Matter **21**, 395502 (2009).

[21] D. Vanderbilt, Phys. Rev. B **41**, 7892 (1990).

[22] J. P. Perdew and W. Yue, Phys. Rev. B **33**, 8800 (1986).

[23] J. P. Perdew, K. Burke, and M. Ernzerhof, Phys. Rev. Lett. **77**, 3865 (1996).

[24] J. P. Perdew and A. Zunger, Phys. Rev. B **23**, 5048 (1981).

[25] Computer Physics Communications **180**, 2582 (2009).

[26] T. N. and M. J. Luriaas, Phys. Rev. B **43**, 1993 (1991).

[27] J. P. Perdew and Y. Wang, Phys. Rev. B **45**, 13244 (1992).

[28] S. Baroni, S. de Gironcoli, A. D. Corso, and e. P. Giannozzi, Rev. Mod. Phys. **73,**, 515 (2001).

[29] A. van de Walle and G. Ceder, Reviews of Modern Physics **74**, 11 (2002).

[30] T. Thomas, D. Pandey, and U. V. Waghmare, Phys. Rev. B **77**, 121203 (2008).

[31] Z. Guo, A. Miodownik, N. Saunders, and J.-P. Schill, Scripta Materialia **54**, 2175 (2006).

[32] R. C. Reed, *The Superalloys* (Cambridge University Press, UK, 2006).

[33] M. J. Donachie and S. J. Donachie, *Superalloys – A Technical Guide*, 2nd ed. (ASM International, Ohio, 2002).

[34] M. Kamaraj, Sadhana **28**, 115 (2003).

[35] C. Rentenberger, T. Waitz, and H. P. Karnthaler, Phys. Rev. B **67**, 094109 (2003).

[36] M. Chandran and S. K. Sondhi, Modelling and Simulation in Materials Science and Engineering **19**, 025008 (2011).

[37] S. Takeuchi, E. Kuramoto, T. Yamamoto, and T. Taoka, Japanese Journal of Applied Physics **12**, 1486 (1973).

[38] P. Veyssiere, J. Douin, and P. Beauchamp, Philosophical Magazine A **51**, 469 (1985).

[39] M. Kolbe, Materials Science and Engineering: A **319321**, 383 (2001).

[40] A. E. Staton-Bevan and R. D. Rawlings, Philosophical Magazine **32**, 787 (1975).

[41] I. Baker and E. M. Schulson, Physica Status Solidi (a) **89**, 163 (1985).

[42] Y. Liu, T. Takasugi, O. Izumi, and H. Ohta, Philosophical Magazine Letters **58**, 81 (1988).

[43] N. Baluc and R. Schublin, Philosophical Magazine A **74**, 113 (1996).

[44] K. J. Hemker and M. J. Mills, Philosophical Magazine A **68**, 305 (1993).

[45] P. Lours, A. Coujou, and B. d. Mauduit, Philosophical Magazine A **62**, 253 (1990).

[46] C. T. Chou, P. B. Hirsch, M. McLean, and E. Hondros, Nature **300**, 621 (1982).

[47] J. R. Rice, Journal of the Mechanics and Physics of Solids **40**, 239 (1992).

[48] G. Dey, Sadhana **28**, 247 (2003).

[49] . Isaev, A. Likhtenshtein, Y. Vekilov, and E. Smirnova, Physics of the Solid State **46**, 1188 (2004).

[50] Y. Wang, Z.-K. Liu, and L.-Q. Chen, Acta Materialia **52**, 2665 (2004).

[51] C. Stassis, F. X. Kayser, C. K. Loong, and D. Arch, Phys. Rev. B **24**, 3048 (1981).

[52] D. M. Clatterbuck, C. R. Krenn, M. L. Cohen, and J. W. Morris, Phys. Rev. Lett. **91**, 135501 (2003).

[53] J. Sun, C. Lee, J. Lai, and J. Wu, Intermetallics **7**, 1329 (1999).

[54] G. E. Dieter, *Mechanical Metallurgy*, 3rd ed. ed. (McGraw-Hill Book Co., New York, 1986).

[55] R. D. Heidenreich and W. Shockley, *Bristol Conf. on Strength of Solids* (The Physical Society, London, 1948), p. 57.

[56] X. Wu *et al.*, Journal of Alloys and Compounds **573**, 1 (2013).

[57] X. An, S. Qu, S. Wu, and Z. Zhang, Journal of Materials Research **26**, 407 (2011).

[58] M. Retima and H. Chadli, Physics Procedia **2**, 1281 (2009).

[59] B. Burton, Acta Metallurgica **30**, 905 (1982).

[60] J. T. Fourie and R. J. Murphy, Philosophical Magazine **6**, 1069 (1961).

[61] W. Z. Han *et al.*, Phys. Rev. Lett. **101**, 115505 (2008).

[62] N. M. Rosengaard and H. L. Skriver, Phys. Rev. B **47**, 12865 (1993).

[63] H. Van Swygenhoven, P. M. Derlet, and A. G. Froseth, Nat Mater **3**, 399 (2004).

[64] M. A. Shehadeh *et al.*, Appl. Phys. Lett **91**, 171905 (2007).

[65] S. Crampin, K. Hampel, D. D. Vvedensky, and J. M. MacLaren, Journal of Materials Research **5**, 2107 (1990).

[66] R. Meyer and L. J. Lewis, Phys. Rev. B **66**, 052106 (2002).

[67] A. van de Walle and G. Ceder, Rev. Mod. Phys. **74**, 11 (2002).

[68] T. Thomas, D. Pandey, and U. V. Waghmare, Phys. Rev. B **77**, 121203 (2008).

[69] S. L. Shang *et al.*, Journal of Physics: Condensed Matter **24**, 155402 (2012).

[70] T. Hickel, B. Grabowski, F. Krmann, and J. Neugebauer, Journal of Physics: Condensed Matter **24**, 053202 (2012).

[71] W. P. Davey, Phys. Rev. **25**, 753 (1925).

[72] J. Hirth and J. Lothe, *Theory of Dislocations* (Wiley Interscience, New York, 1982).

[73] A. Datta, U. Waghmare, and U. Ramamurty, Scripta Materialia **60**, 124 (2009).

[74] S. Ogata, J. Li, and S. Yip, Science **298**, 807 (2002).

[75] J. Wert, X. Huang, and F. Inoko, Proceedings of the Royal Society of London. Series A: Mathematical, Physical and Engineering Sciences **459**, 85 (2003).

[76] D. Alfè, Computer Physics Communications **180**, 2622 (2009).